Three-dimensional crystal plasticity simulations using peridynamics theory and experimental comparison

Aaditya Lakshmanan [a], Jiangyi Luo [b], Iman Javaheri [a,c], Veera Sundararaghavan [a,*]

[a] *Department of Aerospace Engineering, University of Michigan, Ann Arbor, MI, 48105, USA*
[b] *Department of Mechanical Engineering, University of Michigan, Ann Arbor, MI, 48105, USA*
[c] *NASA Langley Research Center, Hampton, VA, 23681, USA*

ABSTRACT

A three-dimensional (3D) peridynamics (PD) model of crystal plasticity (CP) is presented for predicting the fine-scale localization in polycrystalline microstructures undergoing elastoplastic deformation. Microscale data from electron microscopy and digital image correlation have indicated that slip localizations arise early in deformation and act as precursors to mechanical failure and fracture. However, classical numerical approaches such as crystal plasticity finite element methods (CPFEM) are generally unable to predict the emergence and distribution of such localizations. Alternatively, the PD formulation has attracted significant attention for its unique treatment of deformation in the presence of high strain gradient fields. In this paper, a mesh-free non-ordinary state-based PD technique is developed for simulating the elasto-plastic deformation of 3D polycrystalline aggregates of a magnesium alloy. This work presents the details of 3D polycrystal plasticity modeling using PD theory with experimental and CPFEM comparisons. The results from this model are validated against published experimental data for the stress-strain response and texture evolution. The crystal plasticity peridynamic (CPPD) models are successful in simulating grain averaged strains seen in the experiment and depict well-resolved regions of strain localization.

1. Introduction

Developing computational models for microstructure evolution of polycrystalline alloys in industrial applications remains an active challenge. Recent experiments have observed microscale strain localizations, in the form of fine shear bands, on the surface of polycrystals undergoing large deformation using a combination of scanning electron microscopy and digital image correlation (Kammers and Daly, 2013; Guery et al., 2016). These microscale shear bands can act as precursors for damage and failure. These localizations have also been associated with degradation in material strength, in the form of strain-softening (Hornbogen and Gahr, 1975; Bazant et al., 1984). Slip localization naturally occurs in deforming polycrystalline aggregates in the form of lamellar bands of fractions of microns in thickness (Harren et al., 1988). The spacing between such slip bands decreases with increasing plastic deformation (Zhang et al., 2010). Instabilities such as Lüders bands are preceded by strain-softening and advanced by the formation of new slip bands parallel to the old ones(Hallai and Kyriakides, 2013; Yuzbekova et al., 2017; Shaw and Kyriakides, 1997; Jacobs et al.,

---

2019). Micropillar compression experiments (Dimiduk et al., 2006; Greer et al., 2005; Zhang et al., 2013) have revealed plastic behavior characterized by strain bursts under stress-controlled conditions, where such bursts are associated with local strain gradients in the interior of the material (Maaβ et al., 2007). In situ SEM-DIC experiments under monotonic loading also reveal subgrain slip localizations even under positive work hardening rates (Kammers and Daly, 2013; Echlin et al., 2016). (see Figs. 22–24)

Crystal plasticity constitutive models coupled with continuum mechanics have provided a universal framework to model a wide variety of phenomena underlying polycrystalline plasticity (Hill, 1966; Hill and Rice, 1972; Mandel, 1973) and specific applications to modeling localizations. When using the standard crystal plasticity finite element (CPFE) models, the discretization of the volumetric space influences the size of shear bands, resulting in a mesh-dependent method (Anand and Kalidindi, 1994). These models typically require an iterative mesh refinement process to ensure a stable solution. Various enhancements to FEM have been studied in the past to overcome such issues. Early approaches involved the development of traction-separation softening laws whose slope was made to depend on the elemental volume (Oliver, 1989). Later approaches such as extended-FEM (X-FEM) (Samaniego and Belytschko, 2005) or variational multiscale methods (VMM) (Armero and Garikipati, 1996) were developed to represent sharp discontinuities on coarser elements by enriching the finite element interpolations. However, none of the above-mentioned techniques are capable of predicting localization naturally as a consequence of the underlying physics and imperfections are embedded to trigger localization. The development of slip bands and size effect in ductile metals is considered non-local phenomena with an inherent length scale, i.e., the crystallographic slip at a material point is influenced by the deformation of material within a finite neighborhood. A significant body of recent work has employed gradient theories (Counts et al., 2008; Evers et al., 2004; Voyiadjis and Song, 2019; Liu and Dunstan, 2017) to model size effects. These models typically consider strain gradient dependent hardening terms in CP that simulate the evolution of geometrically necessary dislocations (GNDs) (Cermelli and Gurtin, 2001; Acharya et al., 2003). However, such low-order gradient theories do not retain sufficient long-range interactions to model the width and spacing of slip bands accurately. Presumably, the inclusion of higher-order strain gradients could improve the constitutive description, but it would still require a significant amount of calibration at the constitutive level, necessitating costly experiments for detailed dislocation density characterization (Calcagnotto et al., 2010; Ruggles and Fullwood, 2013).

Peridynamics (PD), introduced as an alternative integral formulation to continuum mechanics, is a technique that uses mesh-free and particle-based discretizations (Silling, 2000; Silling et al., 2007). The first version of PD was a bond-based technique in which forces between particles were assumed to be pairwise (i.e., equal and direction-reversed). A more general state-based PD model was subsequently proposed (Silling et al., 2007), where force states were defined by the interactions between the particles. As a result, the non-locality was conveniently introduced without the need to alter the underlying constitutive equations. Here, the deformation measure is computed by integrating the motion of particles across a finite horizon via the correspondence principle. Such an approach has been proven to be exceptionally efficient in modeling discontinuities when compared to continuum mechanics (Madenci and Oterkus, 2014; Gerstle, 2015). In this paper, non-locality is introduced at the level of the governing equilibrium equations via the method of PD (Silling, 2000; Warren et al., 2009). In PD, the body is represented as a set of particles interacting via an integral form of the linear momentum balance equation. Additionally, a state-based theory of PD is implemented where the forces in between particles are computed from stress tensors obtained by CP. The stress tensor at a particle, in turn, is calculated using non-local strains derived by tracking the motion of surrounding particles within a radius of influence. When compared to gradient plasticity theories, this approach is more robust since it can take into account popular CP models of 'local' nature while avoiding higher-order terms at the constitutive level. As a result, the present PD approach is more straightforward since it avoids the need for any additional constitutive model development.

A particular feature of PD has been its ability to effectively model localization in material behavior for a wide variety of problems. These include - but are not limited to - cracks (Ha and Bobaru, 2010; Silling et al., 2010; Agwai et al., 2011), shear bands (Liu et al., 2018; Khan, 2014; Song and Menon, 2018), and phase boundaries (Dayal and Bhattacharya, 2006). However, there has not been much work on microstructural localizations in CP like slip bands, which are very commonly observed at the onset of plasticity in polycrystalline alloys under permanent deformation. Slip band formation in polycrystalline microstructures has been dealt with to some extent (Luo et al., 2018; Sun and Sundararaghavan, 2014a) which base their work on a crystal plasticity peridynamics (CPPD) formulation. These recent studies in CPPD however, have been limited to just two-dimensional (2D) problems. This paper presents the first implementation of PD formulation of CP simulations in three-dimensional (3D) domain with validation against in situ SEM-DIC experiments.

Although PD has been proven effective in the prediction of discontinuities and damage initiations, there are still intrinsic issues of its numerical implementations, among which are zero-energy (also known as hourglass) modes and non-trivial treatment of boundary conditions (BCs) (Breitenfeld et al., 2014; Ren et al., 2016). Recent papers have attempted to resolve the hourglass-like instability by using fictitious springs between the particles (Breitenfeld et al., 2014; Littlewood, 2011). However, these methods have failed to remove the instability altogether. Another branch of methods is to modify the influence functions, either by providing an average-weighted displacement (Wu and Ben, 2015) or by using higher-order approximation of gradients (Yaghoobi and Chorzepa, 2017). In this paper, the latter approach is used to mitigate the zero-energy modes. In addition to the zero-energy modes, non-ordinary state-based PD experiences the difficulty in enforcing BCs (Wu and Ben, 2015). Since PD utilizes an integral-form equation of motion, different from the partial differential equations (PDEs) in conventional continuum mechanics, the enforcement of kinematic
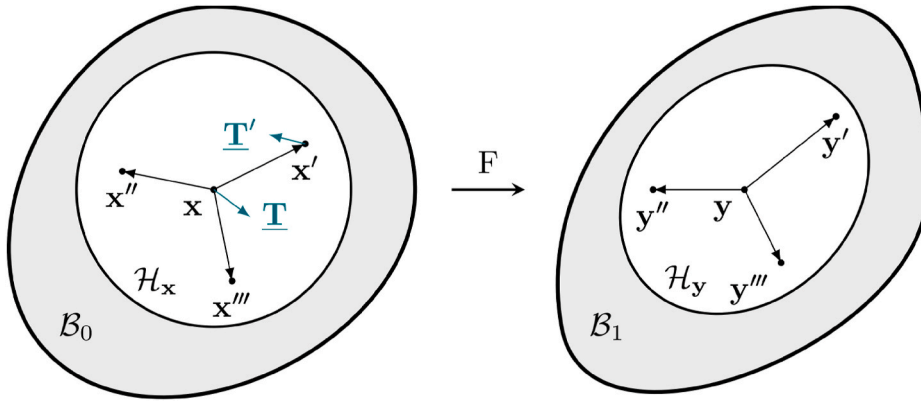
Fig. 1. Kinematics of non-ordinary state-based PD. $\mathcal{B}_0$ is the reference configuration of the body while $\mathcal{B}_1$ is the deformed configuration. The particle at x is bonded to its neighboring particles (positions x', x'', and x''') within a region $\mathcal{H}_x$. The body deforms so that the particle at x displaces to y. The mapping can be described by a corresponding deformation gradient $\mathbf{F}(x, t)$. $\underline{\mathbf{T}} = \underline{\mathbf{T}}[x, t]\langle x' - x\rangle$ and $\underline{\mathbf{T}}' = \underline{\mathbf{T}}[x', t]\langle x - x'\rangle$ are force vector states in the reference configuration associated with particles at x and x', respectively. In the non-ordinary state-based PD theory, these two force vector states are not anti-parallel in general.

constraints at boundaries is not able to follow the standard approach. Here, additional material layers are used to enforce displacement boundary conditions (Sun and Sundararaghavan, 2014b). To obtain a steady state solution, a peridynamics code with an adaptive dynamic relaxation method for quasi-static PD simulations, as detailed in Methodology Section, is implemented (Kilic and Madenci, 2010). Using this approach, an artificial damping ratio estimated from Rayleigh's quotient is selected to dampen the dynamic system. Littlewood (2011) presented an implementation of elasto - crystal viscoplastic material model within the framework of peridynamics very similar to our current work, along with some proof-of-concept simulations carried out using a simple baseline model of a hard inclusion in a single crystal. However, the focus there was to study and compare the material response in the vicinity of a cracked and uncracked particle in single crystals of two different orientations. Gu et al. (2019) presented a non-ordinary state-based PD model of crystal elasto-plasticity with penalty force stabilization which could model fine shear bands in a 2D polycrystalline microstructure with two slip systems. In our current work, a fully explicit implementation of state-based PD for modeling elasto-plastic quasi-static deformation of 3D polycrystals is presented, demonstrating for the first time the capability to simulate polycrystalline mechanical behavior, compare simulation predictions with experimental data and depict well-resolved strain localization. The accuracy and effectiveness of this new dynamic CPPD model is examined by presenting multiple numerical examples.

2. Methodology

In this section, the non-local state-based PD theory is reviewed, followed by a description of the adaptive dynamic relaxation scheme, which is setup by recasting the quasi-static problem as a dynamics problem with artificial damping. Then details on the numerical discretization, solution algorithm and treatment of boundary conditions are presented. Following that, the crystal plasticity constitutive model used to describe elasto-plastic material behavior is detailed.

2.1. Peridynamic formulation

The non-ordinary state-based PD theory forms the theoretical foundation of the present work. This model was first proposed by Silling (Silling et al., 2007) and is a non-local integral reformulation of the classical continuum mechanics theory. Unlike previous bond-based PD models (Silling, 2000; Silling and Askari, 2005) that are restricted to a particular value of the Poisson's ratio, the state-based PD theory can be generalized to include materials with a range of values of the Poisson's ratio. In addition, it is possible to implement classical constitutive material models in the state-based framework, which enabled its integration with crystal elasto-plasticity theory, for this paper.

Consider a material point in the reference configuration at position x, which can only interact with its neighboring points contained in a self-centered horizon $\mathcal{H}_x$ with a finite radius δ. Given the displacement field u of the material point at x, the position of corresponding material point in the current configuration is given by $y = x + u$. We denote the reference configuration of the body as $\mathcal{B}_0$ at time $t = 0$ and the deformed configuration as $\mathcal{B}_1$, as shown in Fig. 1.

Let x' denote the position of a particular material point belonging to $\mathcal{H}_x$, and $\xi = x' - x$ denote a bond. The deformation vector state $\underline{\mathbf{Y}}$ which encodes the kinematics of deformation, maps the bond ξ (in the reference configuration) to its deformed counterpart via $\underline{\mathbf{Y}}[x,$

$t]\langle\boldsymbol{\xi}\rangle = \boldsymbol{y}' - \boldsymbol{y}$. The corresponding deformation gradient tensor, $\mathbf{F}(\boldsymbol{x}, t)$ is defined in terms of $\underline{\mathbf{Y}}[\boldsymbol{x}, t]$ as:

$$\mathbf{F}(\boldsymbol{x}, t) = \left(\int_{\mathcal{H}_x} \omega.(\underline{\mathbf{Y}}[\boldsymbol{x}, t]\langle\boldsymbol{\xi}\rangle \otimes \boldsymbol{\xi}) dV_{x'} \right) \mathbf{K}(\boldsymbol{x})^{-1} \tag{1}$$

where ω is a time-independent influence function defined at particle $\boldsymbol{x}$ in $\mathcal{H}_x$, quantifying the impact of a neighboring particle at $\boldsymbol{x}'$ on the particle at $\boldsymbol{x}$. It is selected as a radially symmetric function which maps the initial bond length to some scalar, i.e., $\omega = \omega(|\boldsymbol{\xi}|)$. $\mathbf{K}(\boldsymbol{x})$ is the shape tensor at $\boldsymbol{x}$, a symmetric and positive-definite tensor, defined as:

$$\mathbf{K}(\boldsymbol{x}) = \int_{\mathcal{H}_x} \omega.(\boldsymbol{\xi} \otimes \boldsymbol{\xi}) dV_{x'} \tag{2}$$

Consequently, The governing equations of PD are formulated as:

$$\rho\ddot{\boldsymbol{u}}(\boldsymbol{x}, t) = \mathbf{L}(\boldsymbol{x}, t) + \boldsymbol{b}(\boldsymbol{x}, t)$$
$$\mathbf{L}(\boldsymbol{x}, t) = \int_{\mathcal{H}_x} \{\underline{\mathbf{T}}[\boldsymbol{x}, t]\langle\boldsymbol{x}' - \boldsymbol{x}\rangle - \underline{\mathbf{T}}[\boldsymbol{x}', t]\langle\boldsymbol{x} - \boldsymbol{x}'\rangle\} dV_{x'} \tag{3}$$

where $\underline{\mathbf{T}}[\boldsymbol{x}, t]\langle\boldsymbol{x}' - \boldsymbol{x}\rangle$ is the force vector state operating on the bond $\boldsymbol{\xi}$, due to the particle at $\boldsymbol{x}$ and time t. Here, $\mathbf{L}(\boldsymbol{x}, t)$ is the summation of the force per unit reference volume due to the interaction of a particle at $\boldsymbol{x}$ with other particles within its horizon. In correspondence with classical continuum theories, the force state $\underline{\mathbf{T}}[\boldsymbol{x}, t]\langle\boldsymbol{x}' - \boldsymbol{x}\rangle$ is related to the first Piola-Kirchoff (PK–I) stress $\mathbf{P}(\boldsymbol{x}, t)$ via the following relation:

$$\underline{\mathbf{T}}[\boldsymbol{x}, t]\langle\boldsymbol{x}' - \boldsymbol{x}\rangle = \omega\mathbf{P}(\boldsymbol{x}, t)\mathbf{K}(\boldsymbol{x})^{-1}.(\boldsymbol{x}' - \boldsymbol{x}) \tag{4}$$

Compared to the governing equations of classical continuum mechanics, no spatial derivatives appear in Eqn. (3) which places fewer restrictions on the regularity properties of deformation descriptors. It is worth noting that despite the current PD model being non-ordinary the balance of angular momentum is ensured due to the relation in Eqn. (4) (Silling et al., 2007; Luo, 2019).

2.1.1. Adaptive Dynamic Relaxation Scheme(ADRS)

In this paper, an adaptive dynamic relaxation method with the quasi-static assumption and a careful time-step selection is adopted. Non-linear problems involving static solutions can alternatively be solved as a dynamics problem through artificial damping, leading to a stable solution through an iterative process. In the absence of body forces, the governing equations shown in Eqn. (3) can be rewritten in a vector form as follows:

$$\ddot{\boldsymbol{u}}(\boldsymbol{x}, t) + c\dot{\boldsymbol{u}}(\boldsymbol{x}, t) = \boldsymbol{f}(\boldsymbol{u}, \boldsymbol{x}, t) \tag{5}$$

where c is a damping ratio coefficient, and the force vector, $\boldsymbol{f}$, is defined as $\boldsymbol{f}(\boldsymbol{u}, \boldsymbol{x}, t) = \boldsymbol{\Lambda}^{-1}\mathbf{L}(\boldsymbol{x}, t)$, in which $\boldsymbol{\Lambda}$ is a diagonal fictitious density matrix. Based on the adaptive dynamic relaxation method, the most desired density matrix and damping coefficient can be determined by Greschgorin's theorem and Rayleigh's quotient, respectively (Kilic and Madenci, 2010).

Let $\boldsymbol{u}^n$, $\dot{\boldsymbol{u}}^n$, $\ddot{\boldsymbol{u}}^n$, and $\boldsymbol{f}^n$ denote the displacement, velocity, acceleration, and force vector field at $t = t_n$, respectively. Here, Δt refers to the time step size. In the central difference scheme, the velocity and acceleration vectors are approximated as:

$$\dot{\boldsymbol{u}}^n \approx \frac{1}{2\Delta t}(\boldsymbol{u}^{n+1} - \boldsymbol{u}^{n-1}) \tag{6}$$

$$\ddot{\boldsymbol{u}}^n \approx \frac{1}{\Delta t^2}(\boldsymbol{u}^{n+1} - 2\boldsymbol{u}^n + \boldsymbol{u}^{n-1}) \tag{7}$$

Hence, substituting Eqns. (6) and (7) into Eqn. (5), and rearranging the terms yields an update scheme for the displacement field:

$$\boldsymbol{u}^{n+1} = \left[2\Delta t^2\boldsymbol{f}^n + 4\boldsymbol{u}^n + (c\Delta t - 2)\boldsymbol{u}^{n-1}\right]/(2 + c\Delta t) \tag{8}$$

Accordingly, Eqn. (9) is employed to approximate $\boldsymbol{u}^{-1}$ for initialization of the displacement update:

$$\boldsymbol{u}^{-1} = \boldsymbol{u}^0 - \Delta t\dot{\boldsymbol{u}}^0 + \frac{\Delta t^2}{2}\ddot{\boldsymbol{u}}^0 \tag{9}$$

where $\boldsymbol{u}^0$, $\dot{\boldsymbol{u}}^0$, and $\ddot{\boldsymbol{u}}^0$ are the initial displacement, velocity, and acceleration vectors, respectively. The velocity and acceleration vectors may be subsequently updated using Eqns. (6) and (7). With the assumption of a unit diagonal matrix $\boldsymbol{\Lambda}$, Δt is selected based on Greschgorin's theorem (Kilic and Madenci, 2010) and is expressed as:

$$\Delta t \leq \sqrt{4\Lambda_{ii}\Big/\sum_j |K_{ij}|} = \sqrt{4\Big/\sum_j |K_{ij}|} = \sqrt{4/\|\mathbf{K}\|_\infty} \tag{10}$$

where $\mathbf{K}$ denotes the stiffness matrix of the system and $\|\cdot\|_\infty$ denotes the vector-induced matrix ∞ norm. Since this stiffness matrix $\mathbf{K}$ is not explicitly computed, another approximation scheme is applied for the time step size. An appropriate value of Δt for the one-
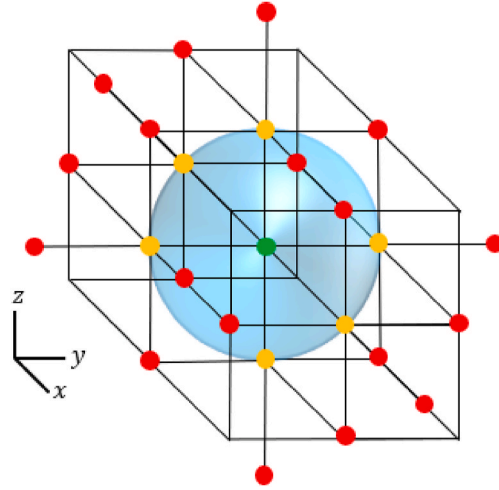
Fig. 2. The green particle is the material point of interest, the yellow particles constitute its nearest neighbors, and the red particles are the nearest neighbors of the yellow particles. Eqn. (18) requires information of the state all the particles marked in the figure. (For interpretation of the references to color in this figure legend, the reader is referred to the Web version of this article.)

dimensional (1D) peridynamic model is based on the wave speed c_s using the Courant-Friedrichs-Lewy (CFL) condition (LeVeque, 2007):

$$\Delta t \leq 2\Delta x/c_s \tag{11}$$

where Δx is the minimal grid size, or the minimal bond length in PD modeling. In higher-dimensional problems, the CFL condition is quite stringent where for an n-dimensional problem using a uniform grid, the critical Δt becomes:

$$\Delta t \leq \frac{2\Delta x}{n}\sqrt{\rho/E_{max}} \tag{12}$$

where ρ is the density, and E_{max} is the largest eigenvalue of the elastic stiffness matrix. Note that the CFL condition in Eqn. (12) can be quite conservative since the derivation is based solely on nearest neighbors (Silling and Askari, 2005). The damping ratio, c, is then selected based on the lowest frequency of the system using Rayleigh's quotient (Kilic and Madenci, 2010):

$$c^n = 2\sqrt{\frac{(u^n)^{\mathrm{T}}k^n u^n}{(u^n)^{\mathrm{T}}u^n}} \tag{13}$$

where k^n is the diagonal local stiffness matrix given by:

$$k_{ii}^n = -(f_i^n/\Lambda_{ii} - f_i^{n-1}/\Lambda_{ii})/(u_i^n - u_i^{n-1}) = -(f_i^n - f_i^{n-1})/(u_i^n - u_i^{n-1}) \tag{14}$$

where f_i^n is the ith component of the force vector, f, at time $t = t_n$. Since the local stiffness matrix calculation involves division by the difference of displacements in consecutive time steps, it is possible to encounter a division by zero. Accordingly the local stiffness k_{ii}^n is set to zero when the difference between displacement fields vanishes. Finally, a guess damping ratio, c_0, is chosen to start computation.

2.1.2. Numerical discretization and algorithm

Assume there are N neighboring particles that lie in the horizon of the particle at x. Neglecting the body force contribution, spatial discretization of Eqn. (3) at time t yields the following:

$$\mathbf{L}(x) = \sum_{i=1}^{N}\{\underline{\mathbf{T}}[x,t]\langle x_i' - x\rangle - \underline{\mathbf{T}}[x_i',t]\langle x - x_i'\rangle\}V_{x_i'} = \mathbf{0} \tag{15}$$

where x_i' is the position i^{th} particle within the horizon of particle at x, with corresponding volume $V_{x_i'}$. The deformation gradient, $\mathbf{F}(x, t)$, and shape tensor, $\mathbf{K}(x)$, are discretized as follows:

$$\mathbf{F}(x,t) = \left[\sum_{i=1}^{N}\omega(y_i' - y) \otimes (x_i' - x)V_{x_i'}\right]\mathbf{K}(x)^{-1}$$

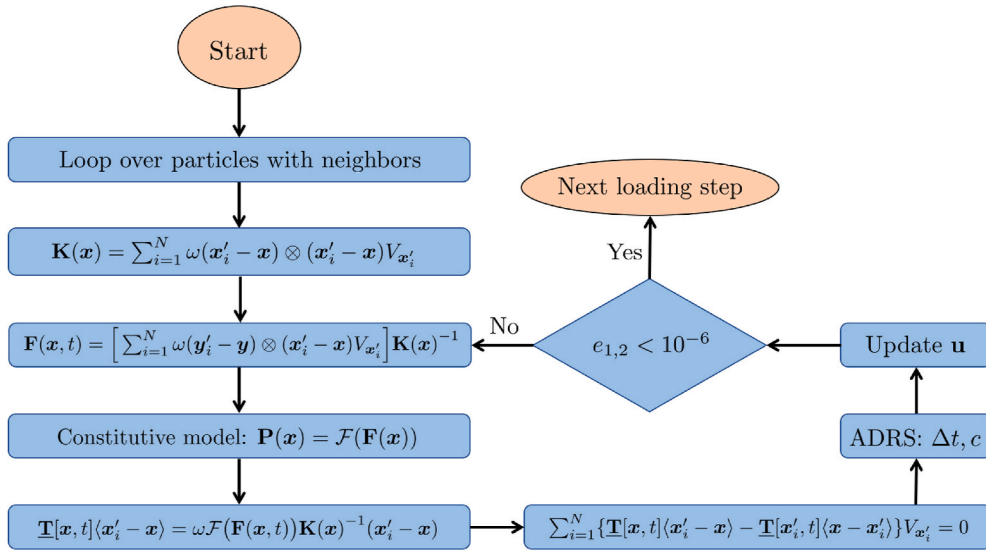$$\mathbf{K}(x) = \sum_{i=1}^{N}\omega(x_i' - x) \otimes (x_i' - x)V_{x_i'} \tag{16}$$
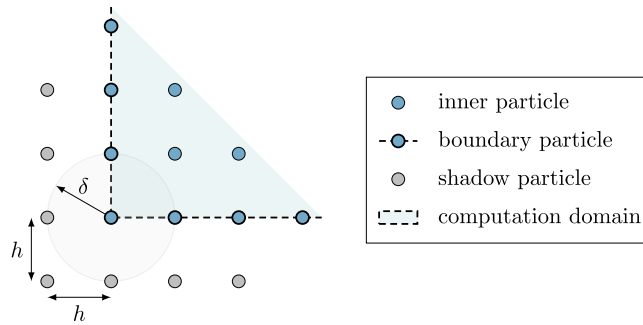
Fig. 3. PD-ADRS flowchart.

Fig. 4. Boundary region with shadow particles depicted in 2D. The thickness of the shadow-particle layer is equal to the horizon size, δ. A horizon of $\delta = h$ is illustrated in this plot, where h is the particle spacing.

where both $\boldsymbol{y}'_i$ and $\boldsymbol{y}$ implicitly depending on t.

Given a particular choice of constitutive model, denoted mathematically by the operator $\mathcal{F}$, the force state $\underline{\mathbf{T}}[x,t]\langle x'_i - x \rangle$ is computed as:

$$\underline{\mathbf{T}}[\boldsymbol{x},t]\langle \boldsymbol{x}'_i - \boldsymbol{x}\rangle = \omega \mathcal{F}(\mathbf{F}(\boldsymbol{x},t))\mathbf{K}(\boldsymbol{x})^{-1}(\boldsymbol{x}'_i - \boldsymbol{x}) \tag{17}$$

where the PK-I stress, $\mathbf{P}(x, t)$, is dictated by the constitutive model through $\mathbf{P}(x,t) = \mathcal{F}(\mathbf{F}(x,t))$. As for the rest half terms in (15), $\underline{\mathbf{T}}[x'_i, t]\langle x - x'_i \rangle$ can be found in a similar manner as shown below:

$$\underline{\mathbf{T}}[\boldsymbol{x}'_i,t]\langle \boldsymbol{x} - \boldsymbol{x}'_i\rangle = \omega \mathcal{F}\left(\mathbf{F}(\boldsymbol{x}'_i,t)\right)\mathbf{K}(\boldsymbol{x}'_i)^{-1}(\boldsymbol{x} - \boldsymbol{x}'_i) \tag{18}$$

However, in order to acquire $\mathbf{F}(x'_i, t)$ and $\mathbf{K}(x'_i)$, the ith particle's horizon needs to be known. Fig. 2 is an illustration of the interactions of a particle with its nearest neighbors and the particles involved in the computation of $\mathbf{L}$.

With all force vector states obtained, the adaptive dynamic relaxation method is applied to solve the discretized version of Eqn. (15). For the 3D problem, the global equations of motion can be organized as a single vector of size $3 \times N_{\text{total}}$, where N_{total} denotes the
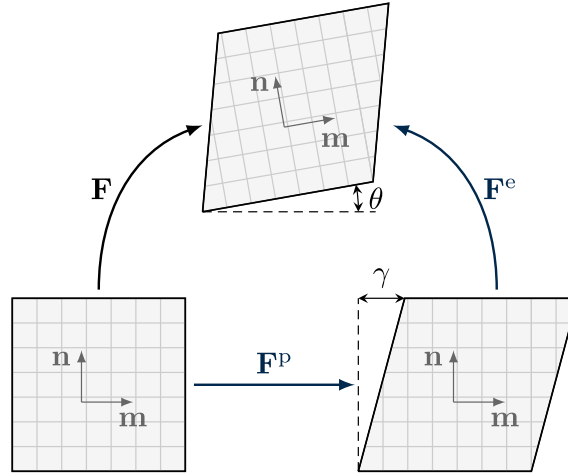
Fig. 5. Schematic of slip systems under deformation gradient $\mathbf{F} = \mathbf{F}^{e}\mathbf{F}^{p}$. $\boldsymbol{m}$ and $\boldsymbol{n}$ are the slip direction and normal vector, respectively. γ is the shear strain due to plastic deformation gradient $\mathbf{F}^{p}$ while θ is the angle of rotation under elastic deformation gradient $\mathbf{F}^{e}$.

total number of particles in the simulation. Since $\mathbf{L}(\boldsymbol{x})$ is completely dependent on the current state, the system is initialized with displacements, velocities, and accelerations. For each iteration of a loading step, two absolute errors ϵ_1 and ϵ_2 are calculated:

$$\epsilon_1 = \frac{\|\mathbf{L}(\boldsymbol{x})\|_2}{N_{\text{total}}} \quad \text{and} \quad \epsilon_2 = \frac{\|\delta\boldsymbol{u}\|_2}{N_{\text{total}}} \tag{19}$$

where Euclidean norm is employed. The error measure, ϵ_1, describes the degree to which the $\mathbf{L}(\boldsymbol{x})$ approaches zero, while ϵ_2 signifies the magnitude of displacement increment between two consecutive iterations. In order to normalize the error from initial guesses, two alternate relative errors e_1 and e_2 are computed and monitored as shown below:

$$e_1 = \frac{\epsilon_1}{\epsilon_1^0} \quad \text{and} \quad e_2 = \frac{\epsilon_2}{\epsilon_2^0} \tag{20}$$

where ϵ_1^0 and ϵ_2^0 refer to the initial absolute errors in each loading step. The iterative process terminates only when both error measures are less than a chosen tolerance, i.e., $e_1 < 10^{-6}$ and $e_2 < 10^{-6}$. All quantities are then updated to proceed with the next loading step. Important computational steps of the PD-ADRS algorithm are summarized in the flowchart shown in Fig. 3. It must be noted that the proposed scheme is simple and general enough to incorporate a variety of constitutive material models.

2.1.3. Boundary treatment

Conventional constraint conditions, such as Dirichlet and Neumann boundary conditions, are imposed in a different form as the PD governing equations are written in non-local formulation. When only nearest-neighbor interactions are considered, no special treatment of boundary conditions is necessary and defect horizons with the smallest horizon can still correctly approximate the deformation gradient close to the boundary. However, as the horizon size increases, irregular defect horizons ultimately lead to disordered and unstable solutions around boundary particles(Macek and Silling, 2007). Since higher-order approximations are derived from internal particles with a fully symmetric horizon and spherically-symmetric influence function, ω, another concern raised is that defect horizons at a boundary will generate errors in approximating the deformation gradient. Based on (Macek and Silling, 2007; Madenci and Oterkus, 2014), a "fictitious material layer" is applied along the boundary where the thickness of this layer is set equal to the horizon size, δ, to ascertain that prescribed constraints are sufficiently forced on the real material region. Shadow particles are then introduced in the fictitious layer, as shown in Fig. 4.

Displacement constraints are implemented in all the numerical examples described ahead. Furthermore, the stresses pertaining to the shadow particles can be computed using the corresponding constitutive model $\mathcal{F}$. These stresses are then utilized in the equations of motion for the boundary particles, even though the boundary particles are prescribed solely with displacements. This special boundary enforcement has been particularly effective when using larger-horizon sizes encompassing particles beyond nearest-neighbors (Luo, 2019).
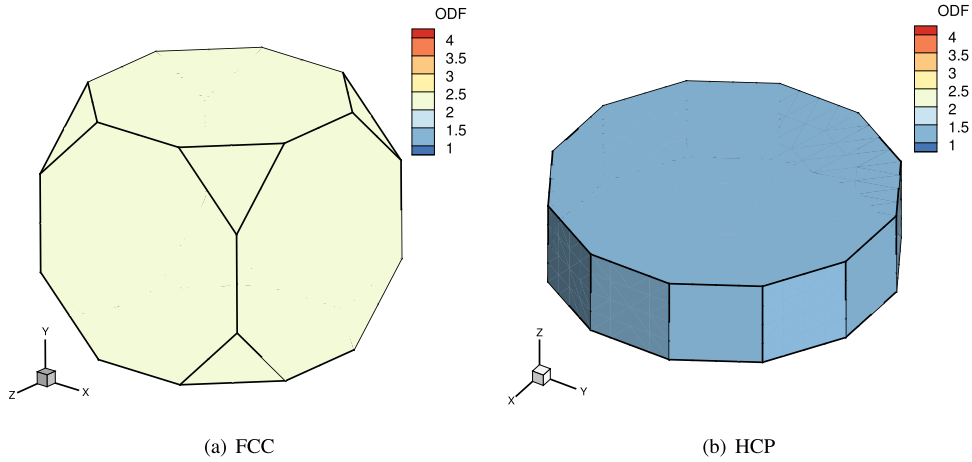
(a) FCC   (b) HCP

Fig. 6. Initial textures of the (a) FCC and (b) HCP polycrystal cubes plotted in the Rodrigues fundamental region while accounting for symmetry.

The most troublesome stability issue of non-ordinary state-based PD is the zero-energy modes (Luo and Sundararaghavan, 2018), which signifies a case where non-unique admissible displacement fields can arise which result in the same deformation gradient and potential energy. Zero-energy modes have been demonstrated to be a material instability rather than a numerical instability in correspondence materials (Silling, 2017). In general, larger horizons exhibit stronger zero-energy modes compared to those of smaller horizons. Those accumulated zero-energy modes, shown as numerical oscillations, can eventually ruin the results and weak couplings between particles is one of the inherent reasons of their occurrence (Breitenfeld et al., 2014; Tupek and Radovitzky, 2014; Wu and Ben, 2015; Yaghoobi and Chorzepa, 2017). The higher-order approximation method first proposed by Yaghoobi and Chorzepa (2017) has been implemented to stabilize zero-energy modes, in which the basic idea is to adjust the weight or influence function values based on the Taylor series expansion to better approximate the deformation gradient.

2.2. Crystal elasto-plasticity theory

Generalized Hooke's law characterizes the elastic behavior of the polycrystal, accompanied by a rate independent CP formulation to model the plastic constitutive behavior (Anand and Kothari, 1996). The deformation gradient, $\mathbf{F}$, forms the primary kinematic descriptor of deformation and assumes a multiplicative decomposition into its constituent elastic, $\mathbf{F}^e$, and plastic, $\mathbf{F}^p$, parts which can be properly expressed as $\mathbf{F} = \mathbf{F}^e\mathbf{F}^p$. Here, dislocation slip on specific slip systems is assumed to be the primary mechanism by which plastic deformation is accommodated. This occurs on a finite number of slip systems which can be completely identified by crystallographic plane normals and directions. A simple schematic of different configurations with the slip systems under deformation is shown in Fig. 5.

The kinematics of plasticity is encoded in the plastic part of the velocity gradient which is expressed as a linear combination of slip rates on individual slip systems as follows:

$$\mathbf{L}^p = \dot{\mathbf{F}}^p\mathbf{F}^{p-1} = \sum_{\alpha}\dot{\gamma}^{\alpha}\mathbf{S}_0^{\alpha}\mathrm{sign}(\tau^{\alpha}) \tag{21}$$

where $\dot{\gamma}^{\alpha}$ is the plastic slip rate, τ^{α} refers to the resolved shear stress, and $\mathbf{S}_0^{\alpha} = \boldsymbol{m}_0^{\alpha} \otimes \boldsymbol{n}_0^{\alpha}$ denotes the Schmid tensor, all corresponding to the αth slip system. Here, sign($\cdot$) denotes the signum function which returns 1 when its argument is positive and 0 otherwise. The elastic constitutive law relates the second Piola-Kirchoff stress (henceforth referred to as the intermediate stress) in the intermediate configuration to the Green-Lagrange elastic strain, which is its elastic power conjugate deformation measure. The intermediate stress is related to the Cauchy stress, $\boldsymbol{\sigma}$, by the relation: $\overline{\mathbf{T}} = \det \mathbf{F}^e\mathbf{F}^{e-1}\boldsymbol{\sigma}\mathbf{F}^{e-T}$. This stress measure is used to compute the resolved shear stress on the αth slip system defined by $\tau^{\alpha} = \overline{\mathbf{T}} \cdot \mathbf{S}_0^{\alpha}$. The elastic constitutive law takes the form $\overline{\mathbf{T}} = \mathcal{L}^e \cdot \overline{\mathbf{E}}^e$, where $\mathcal{L}^e$ is the fourth-order anisotropic elastic stiffness tensor and $\overline{\mathbf{E}}^e$ is the Green-Lagrange elastic strain defined as $\overline{\mathbf{E}}^e = \frac{1}{2}(\mathbf{F}^{eT}\mathbf{F}^e - \mathbf{I})$. To accommodate the phenomenon of strain hardening an evolution equation for the slip system resistance is prescribed as follows (Anand and Kothari, 1996):

Table 1

Elastic constants (Units: GPa) of single crystal FCC copper.

C_{11}	C_{12}	C_{44}
170.0	124.0	75.0

Table 2

Slip resistance and hardening coefficients used for FCC copper.

s_0 (MPa)	h_0 (MPa)	s_s (MPa)	a
16.0	180.0	148.0	2.25

Table 3

FCC copper slip systems.

ID	Direction	Normal	ID	Direction	Normal
1	[1 -1 0]	(1 1 1)	7	[-1 0 1]	(1 -1 1)
2	[-1 0 1]	(1 1 1)	8	[0 –1 -1]	(1 -1 1)
3	[0 1 -1]	(1 1 1)	9	[1 1 0]	(1 -1 1)
4	[1 0 1]	(-1 1 1)	10	[-1 1 0]	(-1 -1 1)
5	[-1 -1 0]	(-1 1 1)	11	[1 0 1]	(-1 -1 1)
6	[0 1 -1]	(-1 1 1)	12	[0 –1 -1]	(-1 -1 1)
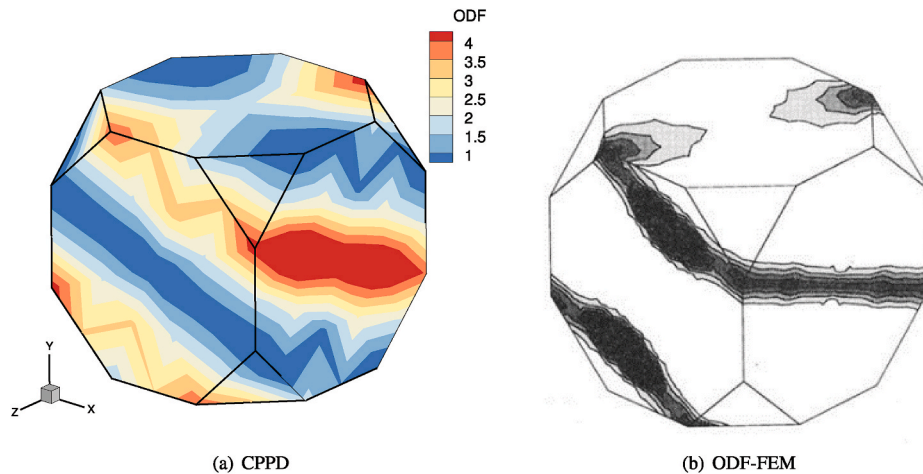
(a) CPPD   (b) ODF-FEM

Fig. 7. Plane-strain compression texture of the 3D FCC polycrystal cube based on (a) CPPD and (b) ODF-FEM (Teodosiu, 1997).

Table 4
Elastic constants (Unit: GPa) of single-crystal HCP magnesium alloy (Hearmon, 1984).

C_{11}	C_{12}	C_{13}	C_{33}	C_{44}
59.3	25.7	21.4	61.5	16.4

Table 5
Mg slip systems (Staroselsky, 1998).

Slip System	ID	Direction	Normal
Basal $< a >$	1	[1 1–2 0]	(0 0 0 1)
	2	[-2 1 1 0]	(0 0 0 1)
	3	[1–2 1 0]	(0 0 0 1)
Prism $< a >$	4	[1–2 1 0]	(1 0–1 0)
	5	[2–1 -1 0]	(0 1 -1 0)
	6	[1 1–2 0]	(-1 1 0 0)
Pyram $< a >$	7	[1–2 1 0]	(1 0–1 1)
	8	[-2 1 1 0]	(0 1 -1 1)
	9	[-1 -1 2 0]	(-1 1 0 1)
	10	[-1 2–1 0]	(-1 0 1 1)
	11	[2–1 -1 0]	(0–1 1 1)
	12	[1 1–2 0]	(1 -1 0 1)
Pyram $< c + a >$	13	[-1 -1 2 3]	(1 1–2 2)
	14	[1–2 1 3]	(-1 2–1 2)
	15	[2–1 -1 3]	(-2 1 1 2)
	16	[1 1–2 3]	(-1 -1 2 2)
	17	[-1 2–1 3]	(1–2 1 2)
	18	[-2 1 1 3]	(2–1 -1 2)
Twin $< c + a >$	19	[-1 0 1 1]	(1 0–1 2)
	20	[1 0–1 1]	(-1 0 1 2)
	21	[-1 1 0 1]	(1 -1 0 2)
	22	[1 -1 0 1]	(-1 1 0 2)
	23	[0–1 1 1]	(0 1 -1 2)
	24	[0 1 -1 1]	(0–1 1 2)

Table 6
Slip constants used for the magnesium alloy (Ganesan, 2017).

Slip System	s_0 (MPa)	h_0 (MPa)	s_s (MPa)	a
Basal $< a >$	76.0	225.6	248.7	1.0
Prism $< a >$	163.2	124.9	356.3	1.0
Pyram $< a >$	160.3	120.2	347.8	1.0
Pyram $< c + a >$	187.4	237.9	350.4	1.0
Twin $< c + a >$	116.4	105.6	238.3	1.0

(a) Plane-strain compression　　　　(b) Uniaxial compression
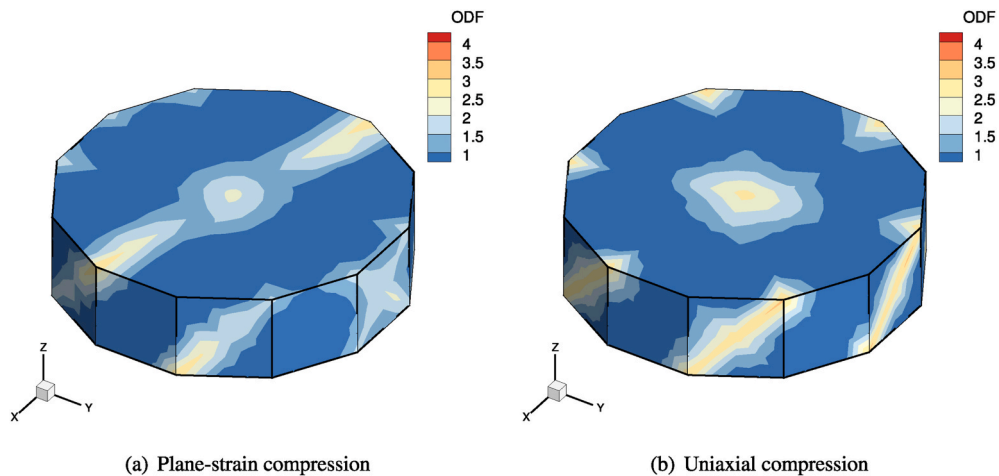
Fig. 8. 3D view of the texture of the 3D HCP polycrystal cube under (a) plane-strain compression, and (b) uniaxial compression.
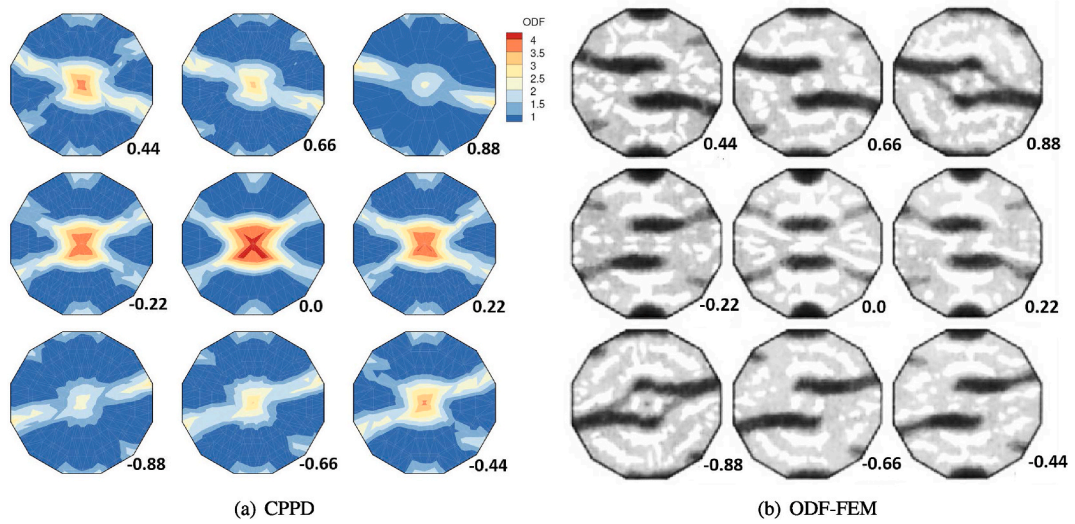
Fig. 9. Plane-strain compression texture of the 3D HCP polycrystal cube based on (a) CPPD and (b) ODF-FEM (Dawson and Marin, 1997). The number to the right corner of each plane indicates the relative position compared to the maximum z-coordinate value in the fundamental region.
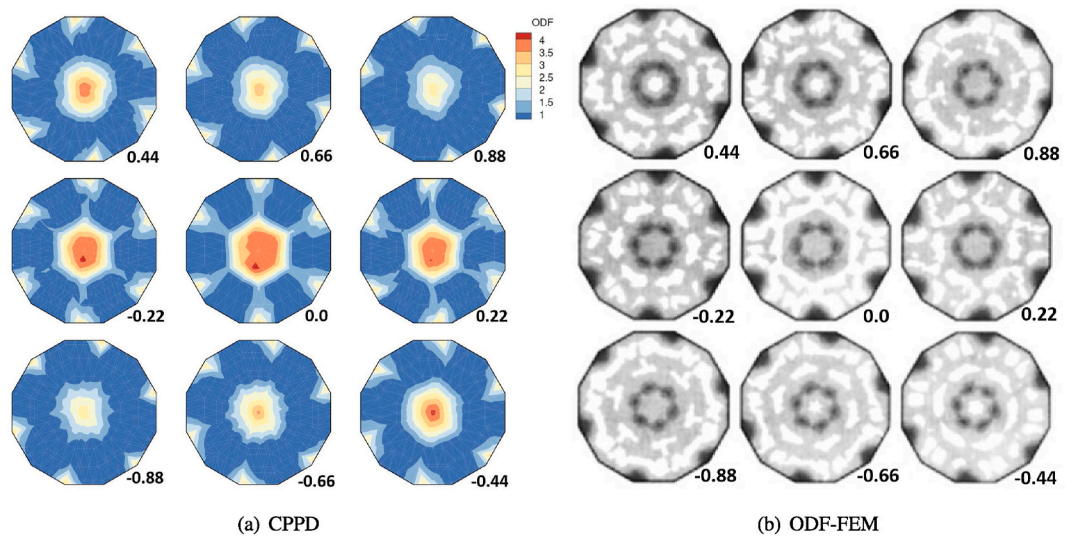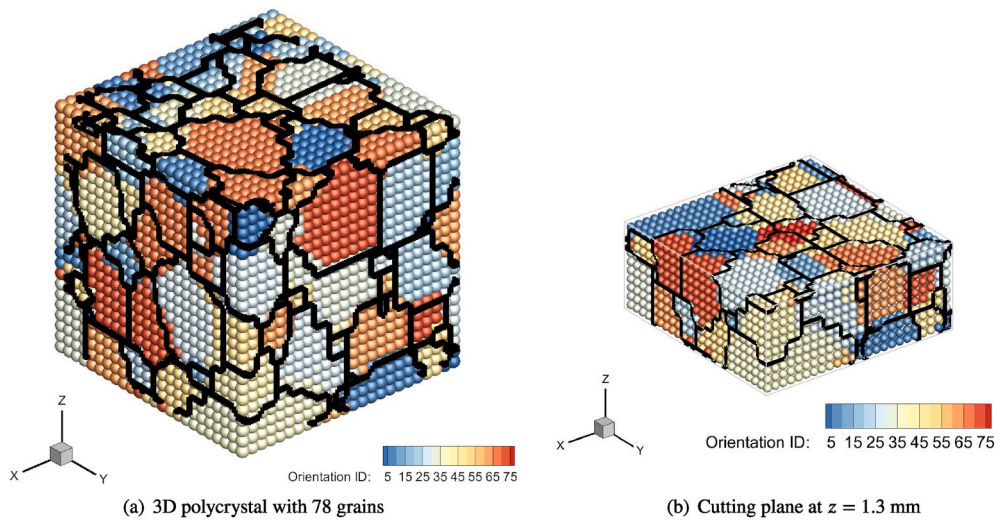

Fig. 10. Uniaxial compression texture of the 3D HCP polycrystal cube based on (a) CPPD and (b) ODF-FEM (Dawson and Marin, 1997). The number to the right corner of each plane indicates the relative position compared to the maximum z-coordinate value in the fundamental region.

(a) 3D polycrystal with 78 grains

(b) Cutting plane at $z = 1.3$ mm

Fig. 11. 3D polycrystal cube with 78 grains. The cube is discretized into particles with a constant inter particle distance h. (a) The example here has 24 particles along all three directions. Grains with the same orientation ID share the same Rodrigues vector. (b) This illustration provides the interior information on the slice $z = 1.3$ mm. The black lines indicate grain boundaries.

(a) Displacement component u

(b) Strain component ϵ_{xx}

(c) Displacement component u

(d) Strain component ϵ_{xx}
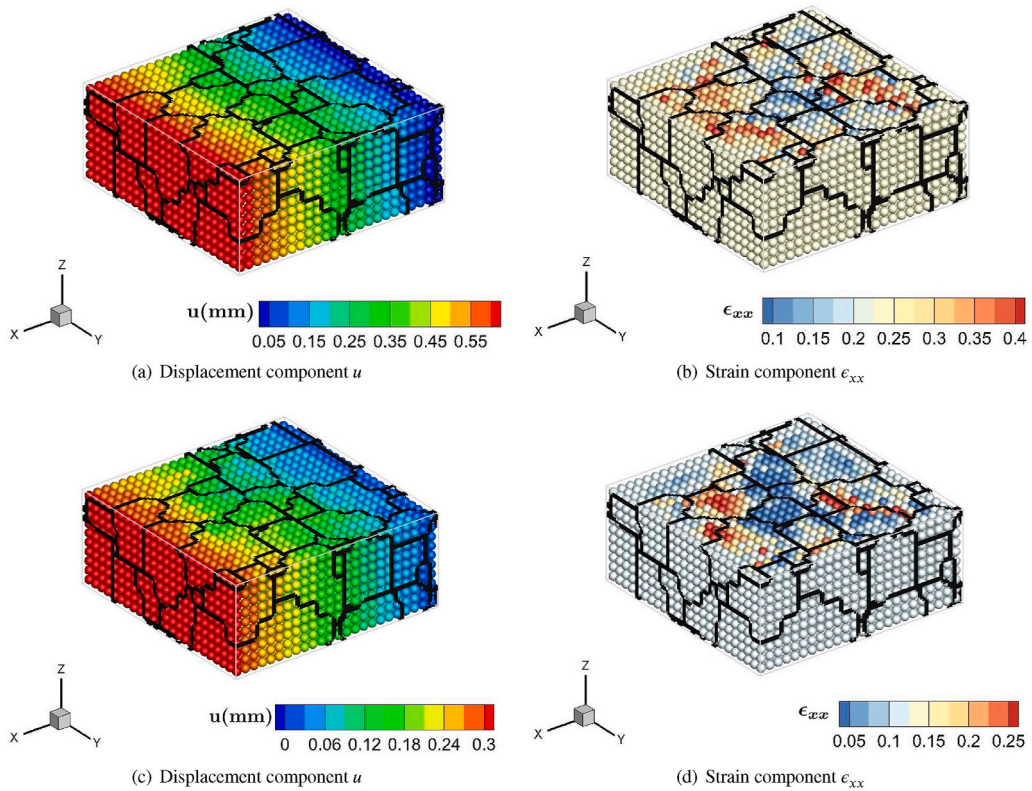
Fig. 12. 3D distributions of displacement component u(in mm), and strain component ε_{xx}, under plane-strain compression(a),(b) and uniaxial compression (c),(d). $\delta = h$. The slices shown here are cut at $z = 1.3$ mm.

(a) $u, \delta = h$

(b) $u, \delta = 2h$

(c) $\epsilon_{xx}, \delta = h$

(d) $\epsilon_{xx}, \delta = 2h$
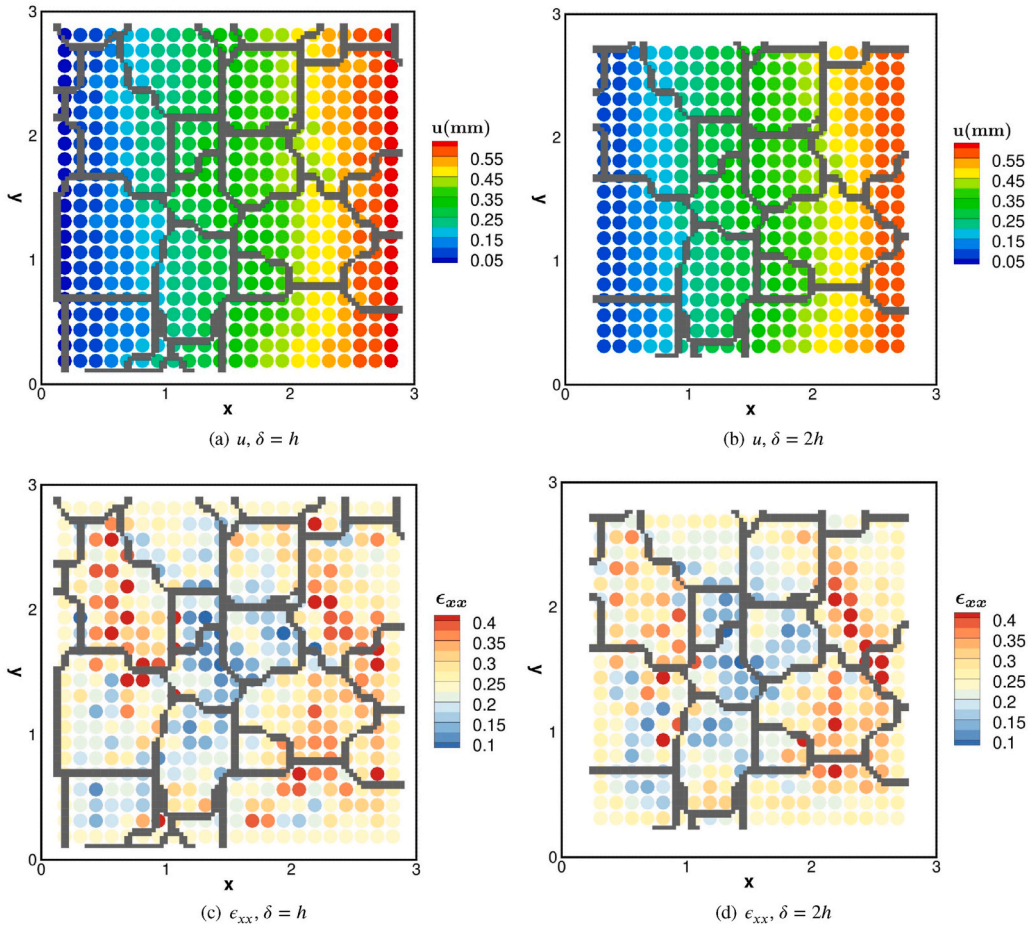
Fig. 13. Displacement component u (in mm), and strain component, ε_{xx}, distributions on the slice $z = 1.3$ mm under plain strain compression. Two different horizon sizes are used. Gray interior lines are grain boundaries.
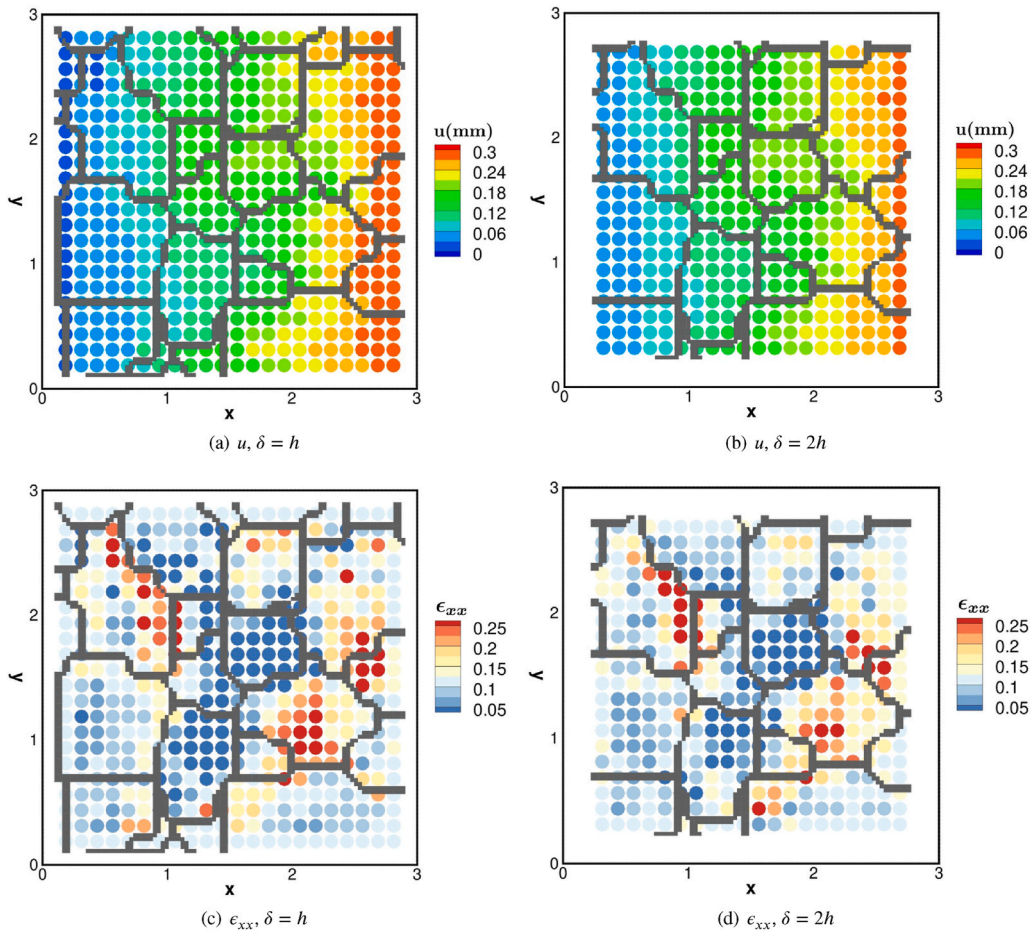
Fig. 14. Displacement component, u, and strain component, ϵ_{xx}, distributions on the slice $z = 1.3$ mm under uniaxial compression. Two different horizon sizes are used. Gray interior lines are grain boundaries.
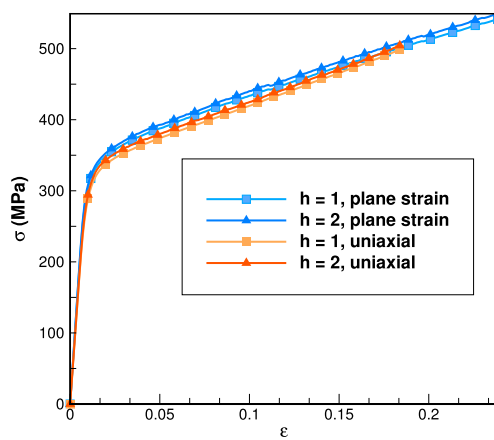
Fig. 15. Homogenized stress-strain responses from plane-strain compression and uniaxial compression using two different horizon sizes.

$$\dot{s}^{\alpha}(t) = \sum_{\beta} h^{\alpha\beta}(t)\dot{\gamma}^{\beta}(t) \; ; \; s^{\alpha}(0) = \tau_0^{\alpha} \tag{22}$$
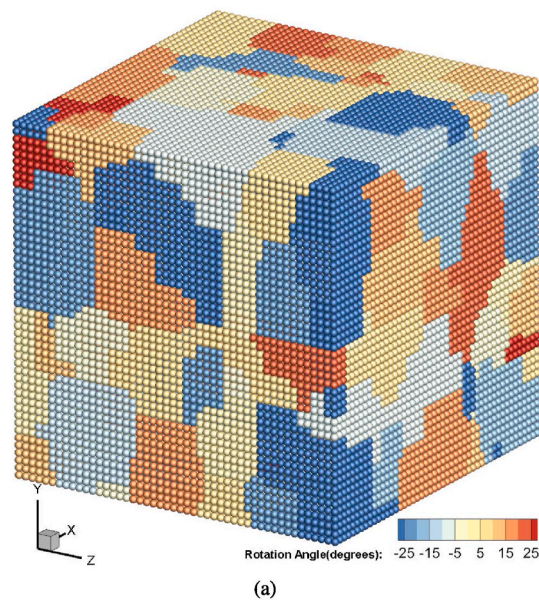
Fig. 16. (a) 3D polycrystal cube discretized into particles with a constant inter particle distance h. There are 48 particles along all three directions. The colormap denotes the anti-clockwise angle of rotation(in degrees) about the z direction relative to the $x - y - z$ coordinate system to achieve the respective orientation.
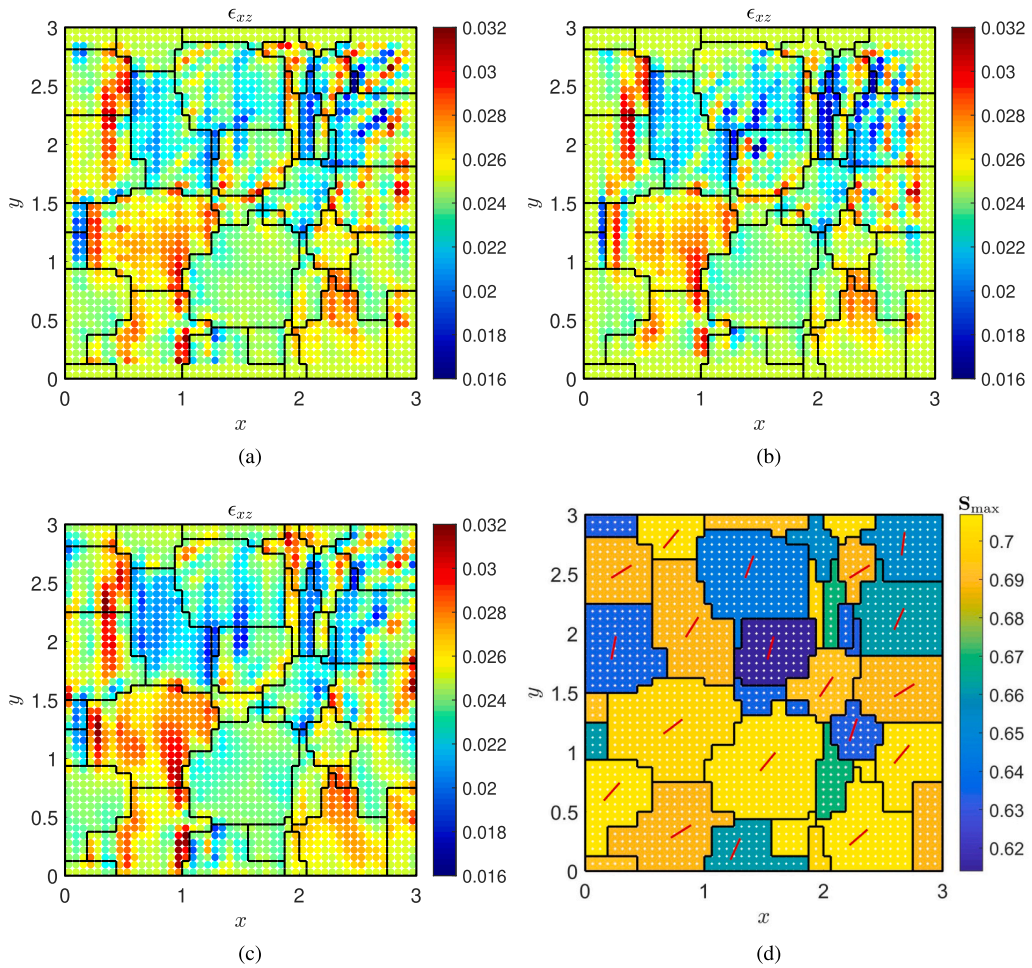
Fig. 17. Shear strain fields at $z = 0.9063$ mm (a)CPPD - ε_{xz}, $\delta = h$ (b)CPPD - ε_{xz}, $\delta = 2h$ (c)CPFE - ε_{xz} (d) Max. Schmid factor plot with red line segments denoting alignment of corresponding basal system. (For interpretation of the references to color in this figure legend, the reader is referred to the Web version of this article.)
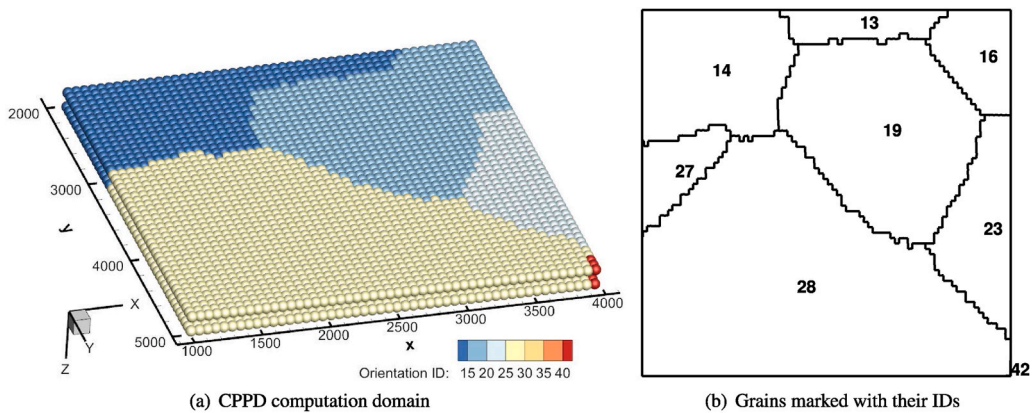
Fig. 18. 3D CPPD computational domain for SEM–DIC image data with 50 particles in x and y directions and 2 slices along z direction. Length dimensions are measured in units of μm. The thickness of the plate is the same as the distance between nearest particles. Units of length are μm.
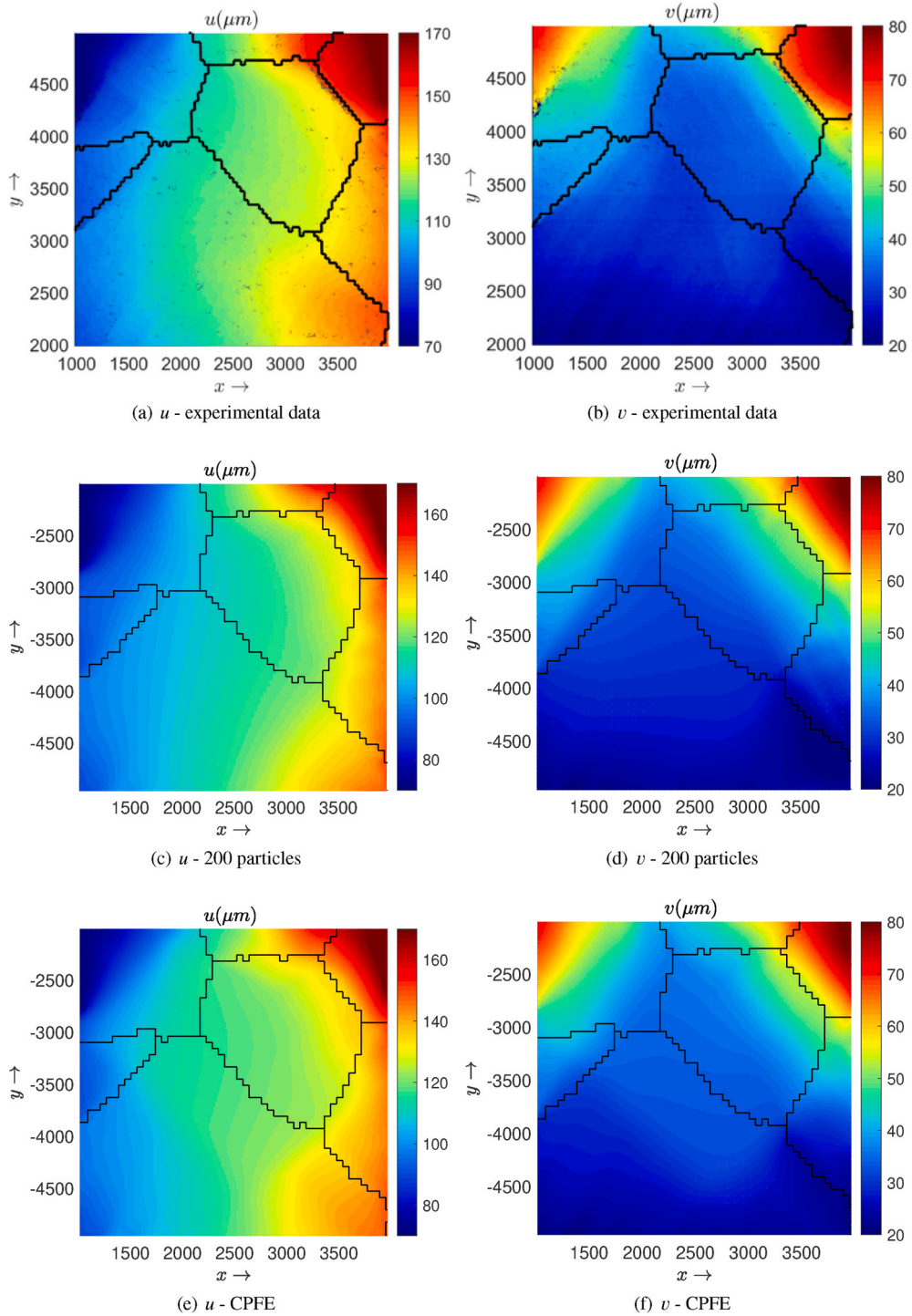
Fig. 19. Displacement components *u* and *v* from SEM-DIC data, CPPD and CPFE. The black segments denote grain boundaries. Units of length are *μm*.

Table 7

Comparison of grain-averaged displacement component u.

Grain ID	u(Exp)	u(200)	Error(%)	u(CPFE)	Error(%)
13	131.214	129.828	1.056	132.353	0.868
14	93.396	93.295	0.109	98.287	5.236
16	161.745	155.732	3.717	155.855	3.642
19	124.381	119.193	4.172	123.614	0.617
23	138.958	137.009	1.403	137.767	0.857
27	96.490	96.784	0.304	100.119	3.761
28	116.7845	112.739	3.464	115.869	0.782

Table 8

Comparison of grain-averaged displacement component v.

Grain ID	u(Exp)	u(200)	Error(%)	u(CPFE)	Error(%)
13	47.1972	47.735	1.139	47.401	0.432
14	46.7184	44.661	4.404	46.238	1.027
16	71.2743	66.812	6.260	67.252	5.644
19	36.3375	37.799	4.022	39.032	7.416
23	33.5344	33.580	0.135	34.459	2.759
27	38.1632	35.923	5.869	36.683	3.8769
28	27.5032	112.739	2.982	28.247	2.705

$$
h^{\alpha\beta}(t) = \begin{cases} h_0^{\beta}\left(1 - \dfrac{s^{\beta}(t)}{s_s^{\beta}}\right)^a & \text{if } \boldsymbol{n}^{\alpha} = \boldsymbol{n}^{\beta} \\[3mm] q h_0^{\beta}\left(1 - \dfrac{s^{\beta}(t)}{s_s^{\beta}}\right)^a & \text{if } \boldsymbol{n}^{\alpha} \neq \boldsymbol{n}^{\beta} \end{cases}
$$

where $h^{\alpha\beta}$ is the hardening coefficient matrix, $\dot{\gamma}^{\beta}(t) > 0$ is the plastic shearing rate on the βth slip system, τ_0^{α} is the initial slip system resistance on the αth slip system, q captures latent hardening, s_s^{β} is the saturation stress on slip system β, and h_0^{β} dictates the maximum value of the hardening coefficient associated with slip system β. The rate-independent CP constitutive model implementation is elaborated in Appendix B, while detailed derivations are presented in Yaghoobi et al. (2019); Ganesan (2017).

3. Results and discussion

The CPPD-ADRS model is validated by comparing its predictions on texture development in polycrystals of two different materials subject to two different deformation modes. This is followed by a demonstration of its capability to model polycrystal plasticity in a more realistic microstructure with two different horizon sizes. We then demonstrate an example of a polycrystal in 3D subject to deformation wherein the ability of CPPD to predict localization band patterns is showcased. Finally the CPPD simulations are investigated for their ability to simulate localization patterns observed in SEM-DIC experimental data of a magnesium alloy, showing some promise as being a single, holistic framework for polycrystalline plasticity modeling.

3.1. Texture comparison under distinct deformation modes

Here, a comparison of texture predictions of CPPD with a finite element implementation of the orientation distribution function (ODF) conservation equation (Teodosiu, 1997) (ODF-FEM) is made. In order to verify the correctness of the CPPD formulation. The microstructure considered here is a 3D polycrystalline cube with a dimension of $3 \times 3 \times 3$ mm^3. The cube is discretized into particles whose centers are separated by a constant distance $h = 0.125$ mm, with 24 particles in each direction, resulting in a total of 13824 particles in the computational domain. Each particle is assigned a unique orientation initially so as to best approximate random texture. The Rodrigues space is accordingly utilized to represent the crystal orientation (Sundararaghavan and Zabaras, 2004, 2007, 2009; Acar and Sundararaghavan, 2016; Javaheri and Sundararaghavan, 2020), in which a rotation can be defined by its axis, $\boldsymbol{n}$, and angle of rotation about that axis, φ. Fig. 6 depicts initial random texture for face-centered cubic (FCC) and hexagonal close packed (HCP) crystals represented in their respective fundamental regions.
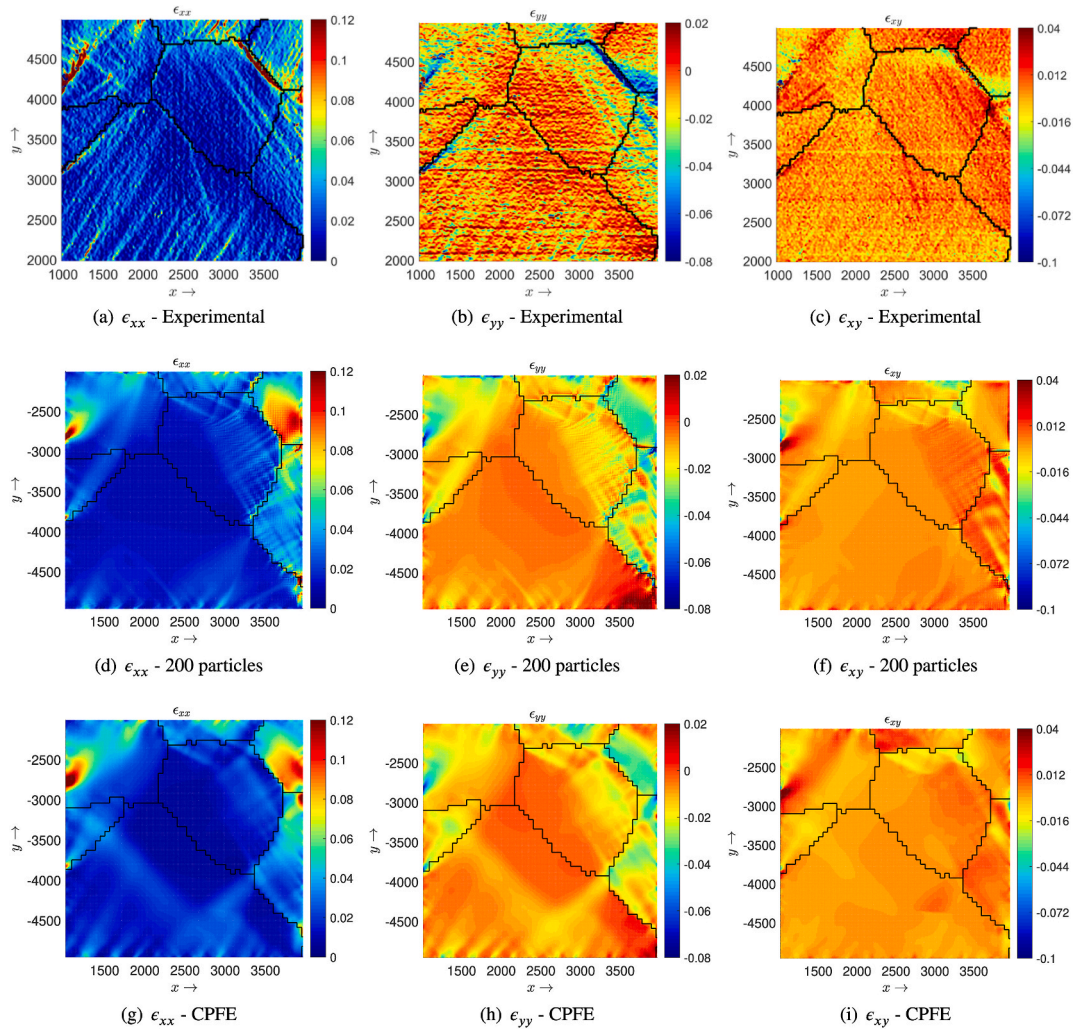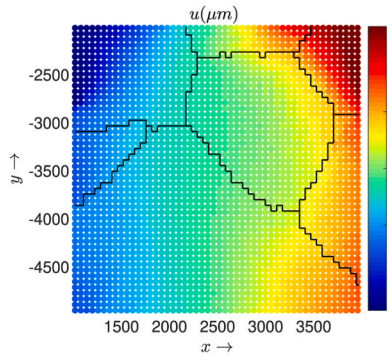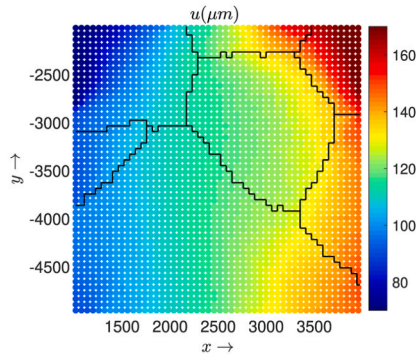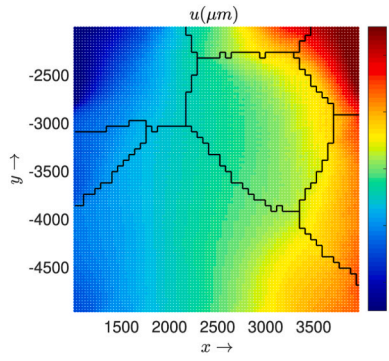
Fig. 20. Strain components ε_{xx}, ε_{yy} and ε_{xy} compared between SEM-DIC data, CPPD with 200 particles and 3 slices, and CPFE. The black segments denote grain boundaries. Units of length are μm.
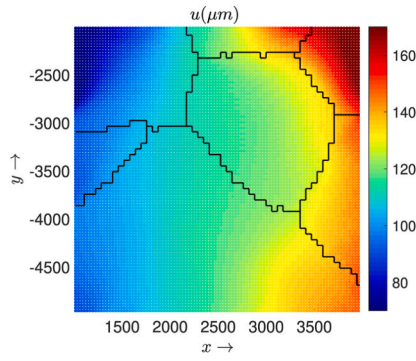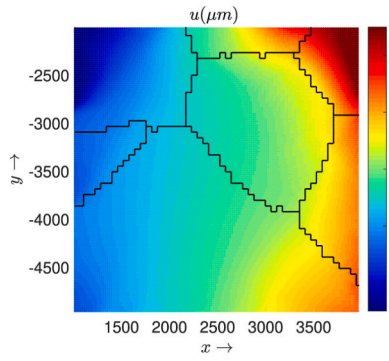
(a) *u* - 50 particles, 2 slices
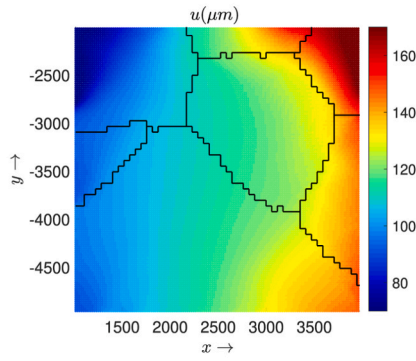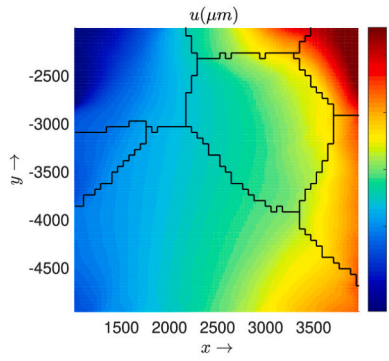
(b) *u* - 50 particles, 3 slices

(c) *u* - 100 particles, 2 slices

(d) *v* - 100 particles, 3 slices

(e) *u* - 150 particles, 2 slices

(f) *v* - 150 particles, 3 slice

(g) *u* - 200 particles, 2 slices
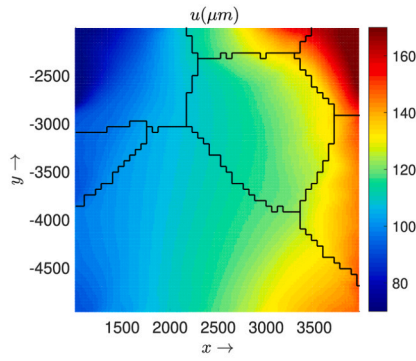
(h) *u* - 200 particles, 3 slices

(caption on next page)

Fig. 21. Displacement component u visualized for different degrees of refinements and number of slices. The black segments denote grain boundaries. Units of length are μm.

The CPPD code is tested in two deformation modes: plane-strain compression and uniaxial compression with initial damping ratio $c_0 = 1$. Both deformation modes allow large strains experimentally(almost unity), since stability limits are not encountered and failure mechanisms such as void growth and coalescence are suppressed (Dawson and Marin, 1997). Displacements enforced on the boundary of the domain are computed from an associated constant velocity gradient tensor. For the plane-strain compression deformation mode, the velocity gradient, $\mathbf{L^{pc}}$, is given by:

$$\mathbf{L^{pc}} = L_0 \begin{bmatrix} 1.0 & 0.0 & 0.0 \\ 0.0 & 0.0 & 0.0 \\ 0.0 & 0.0 & -1.0 \end{bmatrix} \tag{23}$$

where L_0 is a constant signifying the applied strain rate. For uniaxial compression the velocity gradient is set to:

$$\mathbf{L^{ut}} = L_0 \begin{bmatrix} 0.5 & 0.0 & 0.0 \\ 0.0 & 0.5 & 0.0 \\ 0.0 & 0.0 & -1.0 \end{bmatrix} \tag{24}$$

Material parameters chosen for the case of the FCC polycrystal correspond to copper (Anand and Kothari, 1996). The elastic constants and hardening coefficients for the CP model are given in Tables 1 and 2, while the twelve slip systems are listed in Table 3. All slip systems being crystallographically symmetric are assumed to share the same slip resistance and hardening coefficients.

For the copper polycrystal, only the plane-strain compression test is conducted where $L_0 = 0.001s^{-1}$ is imposed over 200 deformation steps. Fig. 7 provides a comparison of texture of the FCC polycrystal post-deformation between CPPD and ODF-FEM, which agree well qualitatively.

Next, two test cases and examples for HCP polycrystals are shown. Magnesium alloy WE43-T5 temper is chosen for this study, and its elastic constants are given in Table 4. 18 slip systems for this alloy are considered, including 3 basal $< a >$, 3 prismatic $< a >$, 6 pyramidal $< a >$, and 6 pyramidal $< c + a >$ slip systems. No twin systems, however, are considered for this case study. Tables 5 and 6 include the slip systems and hardening coefficients respectively, used for this test case.

Two modes of deformation, i.e., plane-strain compression and uniaxial compression are imposed with $L_0 = 0.001s^{-1}$ over 200 deformation steps. In order to compare CPPD textures with the those computed by ODF-FEM from (Dawson and Marin, 1997), a 3D view of the texture, as shown in Fig. 8, is used. The fundamental region is then sliced to compare the interiors. The same slices are selected for ODF-FEM and CPPD results and are depicted in Figs. 9 and 10. Here, all CPPD results are based on a horizon size that includes only the nearest particles (i.e., $\delta = h$).

ODF-FEM textures exhibit more smooth and symmetric texture, while the CPPD results show visible numerical oscillations due to the explicit scheme. Overall, the textures are qualitatively similar under both deformation modes, which indicates the capability of the 3D CPPD-ADRS implementation to satisfactorily capture the deformation textures for FCC and HCP polycrystals.

3.2. Polycrystalline microstructure simulation

A 3D polycrystalline cube with 78 grains and properties of WE43 alloy-T5 temper, shown in Fig. 11, forms the microstructure of interest with dimensions $3 \times 3 \times 3$ mm^3. Simulations are performed with two different horizon sizes, i.e., $\delta = h$ and $\delta = 2h$ with initial damping ratio $c_0 = 1.0$.

The plane-strain compression velocity gradient, $\mathbf{L^{pc}}$, and uniaxial compression velocity gradient, $\mathbf{L^{ut}}$, are applied on the boundary, using a constant strain rate $L_0 = 0.001s^{-1}$. The displacement and strain maps captured at the 200th deformation step are depicted in Fig. 12 for plane-strain and uniaxial deformation.

The slice $z = 1.3$ mm is used to compare the displacement and strain contours for different horizon sizes. Figs. 13 and 14 depict the contours of the x-component of displacement, u, and normal strain, ε_{xx}, for the two different horizon sizes under plane-strain compression and uniaxial compression, respectively. The shadow particles along the boundary are masked, leading to margins on all four sides depending on the horizon size. All particles within the horizon distance of the boundary are classified as shadow particles, and hence this layer becomes thicker with increasing the horizon size. Results obtained from larger horizons exhibit smoother variation of displacement and strain, which may be attributed to the higher-order approximation method, which effectively suppresses zero-energy mode oscillations. Finally the particle density is increased to investigate the convergence of the homogenized stress-strain curves with larger horizons. Fig. 15 shows that stress-strain curves almost coincide for the two different horizon sizes, with a higher stress for larger horizon as compared to smaller horizon for the same strain. This observation is attributed to different thickness of the shadow particle layers for larger horizon sizes where the simulation domain is effectively smaller.
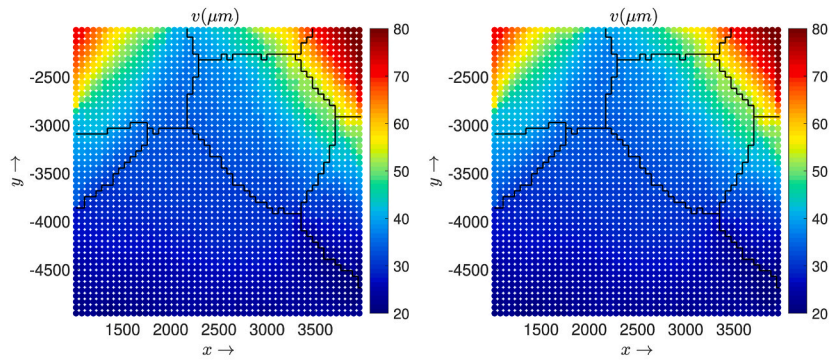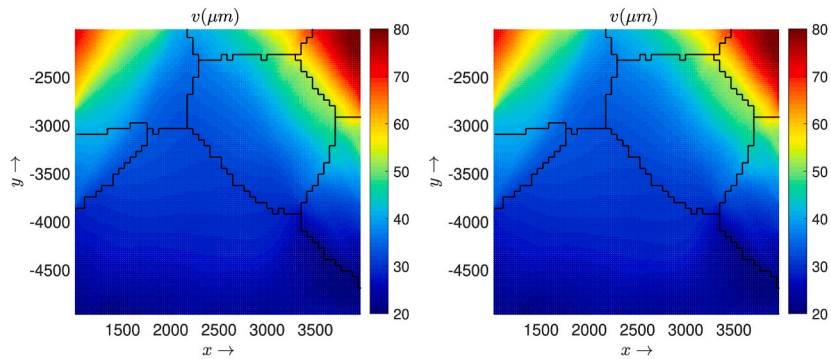
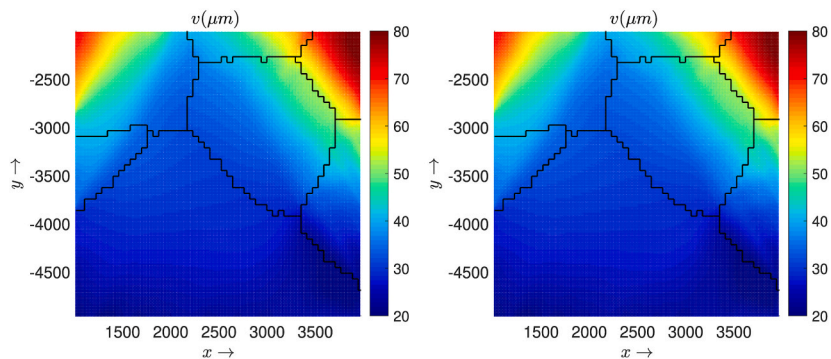(a) v - 50 particles, 2 slices

(b) v - 50 particles, 3 slices
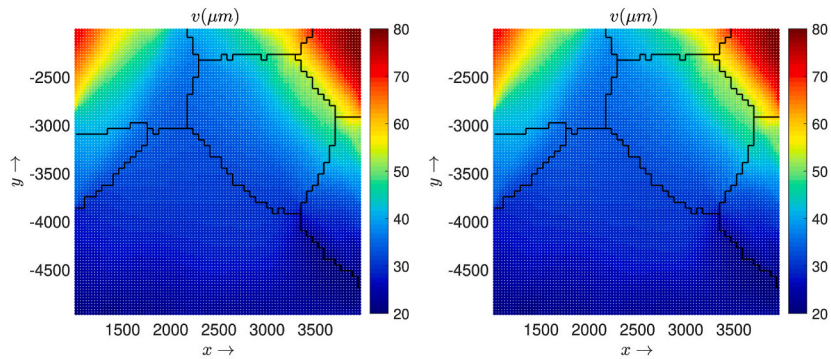
(c) v - 100 particles, 2 slices

(d) v - 100 particles, 3 slices

(e) v - 150 particles, 2 slices

(f) v - 150 particles, 3 slices

(g) v - 200 particles, 2 slices

(h) v - 200 particles, 3 slices

(caption on next page)

Fig. 22. Displacement component v visualized for different degrees of refinements and number of slices. The black segments denote grain boundaries. Units of length are μm.

3.3. 3D CPPD simulations with basal slip

A 3D polycrystalline cube with properties of WE43 alloy-T5 temper(Tables 4 and 6), shown in Fig. 16(a) forms the microstructure of interest with dimensions $3 \times 3 \times 3$ mm^3 and 48 particles in each direction. Orientations are chosen in a way that the z direction coincides with the basal plane normal for all orientations, and hence, orientation pairs are related to one another via a rotation about the z direction. Displacement boundary conditions are applied based on the following velocity gradient

$$\mathbf{L}^s = L_0 \begin{bmatrix} 0 & 0 & 1 \\ 0 & 0 & 1 \\ 0 & 0 & 0 \end{bmatrix} s^{-1} \ , \ L_0 = 0.001 \ s^{-1} \tag{25}$$

The motivation for choosing the prescribed set of orientations as earlier along with the velocity gradient, $\mathbf{L}^s$, was to initiate specifically basal slip, and for this example only the basal slip systems are assumed to be active. The simulation is performed for 50 deformation steps with horizon sizes $\delta = h$ and $\delta = 2h$, with the initial damping ratio $c_0 = 1.0$.

For further analysis we consider the specific case of the section $z = 0.9063$ mm, for which the shear strain fields are depicted in Fig. 17. For comparison with predictions of CPFE the equivalent problem was setup in the PRISMS-CPFE (Yaghoobi et al., 2019) framework on a $3 \times 3 \times 3$ mm^3 polycrystal idealized as a structured grid with 48^3 hexahedral elements and the same orientations assigned to mesh elements as the CPPD problem. The same crystal plasticity constitutive model was employed with material properties, slip constants and hardening parameters identical to the CPPD problem. Displacement boundary conditions were enforced on the boundary based on the velocity gradient $\mathbf{L}^{s'}$ below

$$\mathbf{L}^{s'} = L_0 \begin{bmatrix} 0 & 0 & 1 \\ 0 & 0 & 1 \\ 0 & 0 & 0 \end{bmatrix} \ , \ L_0 = 0.0001 \ s^{-1} \tag{26}$$

To achieve the same macroscopic strain level as the CPPD, the CPFE simulation was performed over 500 deformation steps. Additionally we define a Schmid factor for the current scenario as follows:

$$\mathbf{S}_i = |\widehat{\boldsymbol{\sigma}} : (\boldsymbol{m}_i \otimes \boldsymbol{n})| ; \ i \in \{1, 2, 3\} \ , \ \widehat{\boldsymbol{\sigma}} = \begin{bmatrix} 0 & 0 & 0.5 \\ 0 & 0 & 0.5 \\ 0.5 & 0.5 & 1 \end{bmatrix} \tag{27}$$

where i denotes the index of the basal slip system under consideration and $\widehat{\boldsymbol{\sigma}}$ is a 'unit' stress tensor representative of the deformation mode. $\boldsymbol{m}_i$ is the slip direction corresponding to the ith basal slip system in the $x - y - z$ coordinate system and $\boldsymbol{n}$ is the slip plane normal, which in the present case coincides with the z direction. The form of $\widehat{\boldsymbol{\sigma}}$ is motivated by the following construction. Given $\mathbf{L}^s$ the global deformation gradient is computed as

$$\mathbf{L}^s = \mathbf{F}_g \mathbf{F}_g^{-1} \Longrightarrow \mathbf{F}_g(t) = \exp(t\mathbf{L}^s)\mathbf{F}(0) \Longrightarrow \mathbf{F}_g = \mathbf{I} + t\mathbf{L}^s \tag{28}$$

where $\exp(\cdot)$ denotes the matrix exponential and $\mathbf{I}$ denotes the identity matrix. Note that from the chosen form of $\mathbf{L}^s$ which satisfies $\mathbf{L}^s \cdot \mathbf{L}^s = \mathbf{0}$ and using $\mathbf{F}_g(0) = \mathbf{I}$ we obtain $\mathbf{F}_g(t)$. Then the global Green-Lagrange strain tensor takes the form

$$\mathbf{E}_g = \frac{1}{2}\left(\mathbf{F}_g^T \mathbf{F}_g - \mathbf{I}\right) = \frac{1}{2}\left((\mathbf{I} + t\mathbf{L}^s)^T . (\mathbf{I} + t\mathbf{L}^s) - \mathbf{I}\right) = \frac{1}{2}\left(t\mathbf{L}^{sT} + t\mathbf{L}^s\right) = t \begin{bmatrix} 0 & 0 & 0.5 \\ 0 & 0 & 0.5 \\ 0.5 & 0.5 & 1 \end{bmatrix} \tag{29}$$

If we define a global stress measure using $\mathbf{E}_g$ and an effectively transversely isotropic material(about z direction), the global stress measure will also take a form similar to $\mathbf{E}_g$. Since time and the effective material constants appear purely as scaling parameters, $\widehat{\boldsymbol{\sigma}}$ takes the form suggested in Eqn. (27). Note however, that the number 1 appearing in $\widehat{\sigma}_{zz}$ does not affect the computation of $\mathbf{S}_i$ because it appears in Eqn. (27) after multiplication with $(\boldsymbol{m}_i \otimes \boldsymbol{n})_{zz}$ which is 0 because $\boldsymbol{m}_i$ is a vector completely contained in the $x - y$ plane. Subsequently, we define the maximum Schmid factor as $\mathbf{S}_{\max} = \max\limits_{i} \{\mathbf{S}_i\}$.

Fig. 17(d) depicts the maximum Schmid factor plot for the section. CPPD shows some signatures of localization bands forming in grains with low Schmid factor, also observed in the CPFE results, while the grains with highest Schmid factor show almost uniform strain. Such an observation was also made by Luo et al. (2018) and Sun and Sundararaghavan (2014b), drawing a major conclusion that shear band formation is a favorable deformation mode in grains with a low Schmid factor. CPPD results for both horizon sizes
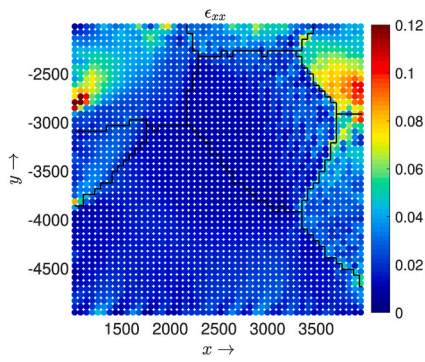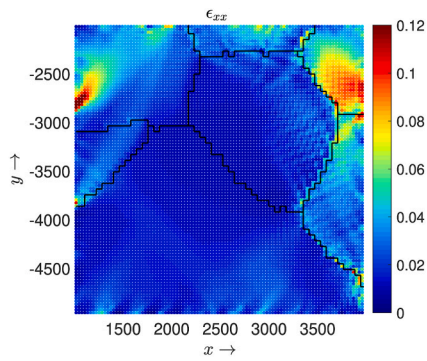
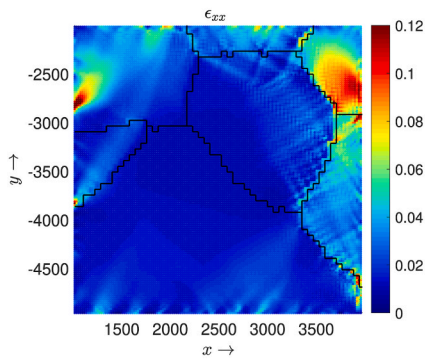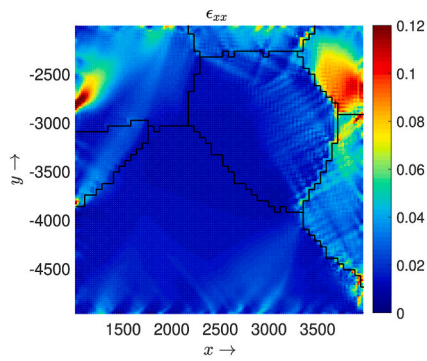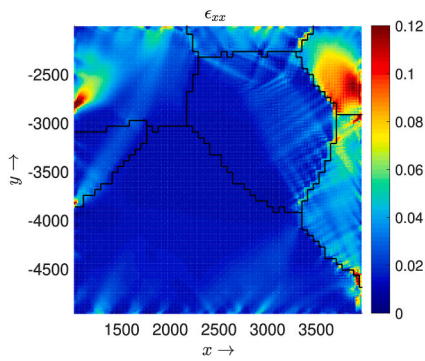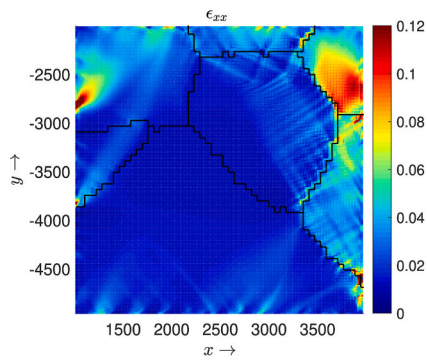(a) ϵ_{xx} - 50 particles, 2 slices
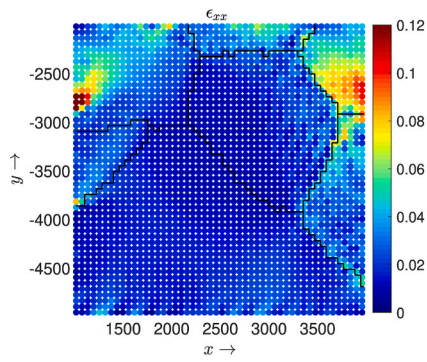
(b) ϵ_{xx} - 50 particles, 3 slices
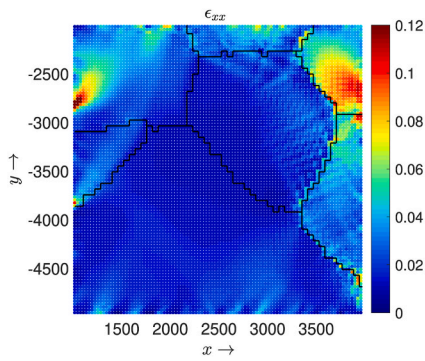
(c) ϵ_{xx} - 100 particles, 2 slices

(d) ϵ_{xx} - 100 particles, 3 slices

(e) ϵ_{xx} - 150 particles, 2 slices

(f) ϵ_{xx} - 150 particles, 3 slices

(g) ϵ_{xx} - 200 particles, 2 slices

(h) ϵ_{xx} - 200 particles, 3 slices

(caption on next page)

Fig. 23. Strain component ε_{xx} visualized for different degrees of refinements and number of slices. The black segments denote grain boundaries. Units of length are μm.

agree well in a qualitative sense with CPFE, showcasing the applicability of implementation of classical crystal plasticity constitutive models in a peridynamics framework.

3.4. CPPD simulations vs SEM-DIC experimental data

Here, the CPPD framework predictions are compared with state-of-the-art in situ SEM-DIC data of WE43 magnesium alloy (Githens et al., 2020a). SEM–DIC is a useful in-situ, non-destructive technique for characterizing microscopic surface strains. A speckle pattern placed on the microstructure during thermomechanical loading is tracked by the DIC setup which is then post-processed to obtain the surface displacement fields, from which the surface strains can be computed. Details of the SEM-DIC experiments that were performed for the WE43 alloys are described in greater detail by Ganesan (2017); Githens et al. (2020b); Ganesan et al. (2021). The primary material used for the experiments was a hot-rolled annealed WE43 plate with a thickness of 31 mm, subjected to T5 temper condition. Electron backscatter diffraction (EBSD) scans of the surface prior to loading were used to extract grain orientation information. Intergranular and intragranular strain localization patterns are widely observed throughout the microstructure under tensile loading, while no twinning is recorded. The comparison of CPPD with experimental results for the above experiment is examined.

The mechanical test is modeled using CPPD as a boundary value problem (BVP) using the EBSD map of the microstructure within the DIC window. The displacement of the boundary of the microstructure is obtained from experiments and these are used to setup displacement BCs on the lateral boundaries. Measurements are made on the surface of the sample, which is a traction-free surface, and hence, the top and bottom surfaces in the simulation are traction-free. For the sake of comparison with an FE implementation, the same problem is simulated using the PRISMS-CPFE framework(Yaghoobi et al., 2019).

Fig. 18 provides an example of the CPPD computational domain. The thickness of the plate is set equal to the distance between the nearest particles, while the horizon size is set equal to the smallest inter-particle distance. The four sides of the plate are displacement-constrained based on DIC experimental data. In each loading step, 0.2% of the final displacement is imposed so that 500 displacement increments are used arrive at the total displacement. In addition, the bottom surface is constrained only in the z-direction. Simulations are performed with four degrees of refinement on the particle grid: 50, 100, 150 and 200 particles, in both x and y directions. Additionally, for each level of refinement, 2 and 3 slices of particles are constructed so that 8 different cases are simulated in total. The initial damping ratio is set to $c_0 = 0.5$.

The corresponding FEM problem involves a 200 × 200 x 1 grid with displacement BCs on the lateral boundaries(obtained from experiment) and the remaining two surfaces being traction-free. The final displacement on the boundary is achieved in 1000 simulation steps using the same constitutive model and parameters as done for the CPPD simulations.

Tables 4 and 6 contain the elastic constants, slip systems, and slip system hardening constants used for the CPPD simulations. It is to be noted that the $< c + a >$ slip system is the only one capable of accommodating strains along the c-axis, but it is also difficult to activate at room temperature due to the high initial slip resistance (Acar et al., 2017). Twinning is an additional mode that can accommodate deformation along the c-axis at the expense of a strong asymmetry in mechanical properties. In magnesium alloys, the extension twinning system (which leads to a tensile strain parallel to the c-axis) is activated during an in-plane compression, followed by an increase in hardening at higher strains (due to twin exhaustion). Tensile twins significantly affect the texture by reorientation of the grains by an angle of about $86°$, which makes it necessary to include twinning in the CP constitutive model. For the present work, twin systems are considered as pseudo-slip systems, undergoing shear deformation until they reorient (Tomé and Kaschner, 2005). The total twin volume fraction, which is the total accumulated pseudo-slip divided by the characteristic shear of the twin system, is computed for each particle. In magnesium, extension twins are active in compression with a characteristic shear of 0.129. An approach similar to the Predominant Twin Reorientation(PTR) scheme (Tomé and Kaschner, 2005) is used with the main difference being that individual particles are reoriented when a threshold twin volume fraction is attained, instead of reorienting the entire grain that the particle belongs to.

Fig. 19 depicts the comparison of the x and y components of displacement between experimental data, CPPD simulations(using 200 particles and 3 slices) and CPFE simulation. Tables 7 and 8 tabulates the grain averaged displacement components. Very good match is obtained for the grain-averaged displacement field predictions between CPPD, CPFE and experiments, as evidenced by the percentage difference with experiment. This affirms, on a first level, the ability of the CPPD framework to solve elasto-plastic BVPs directly comparable with experimental measurements. Figs. 21-22 depict the variation of x and y components of displacement respectively, for different degrees of refinement and number of slices.
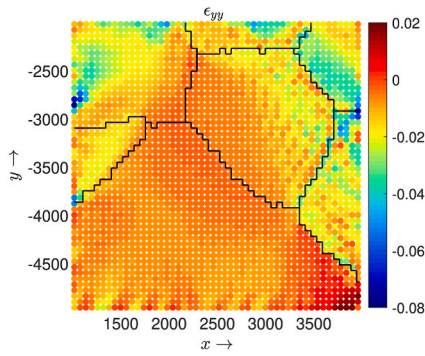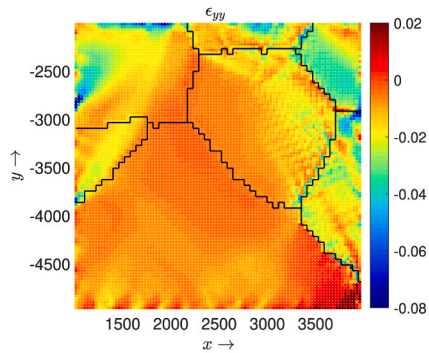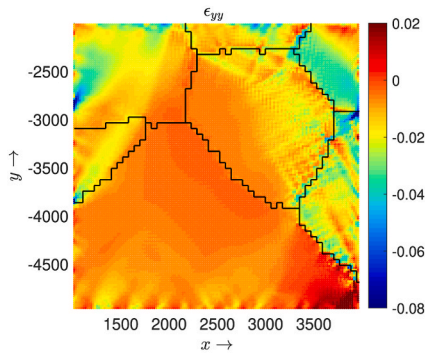
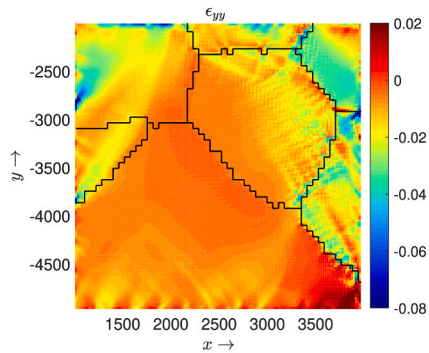(a) ϵ_{yy} - 50 particles, 2 slices
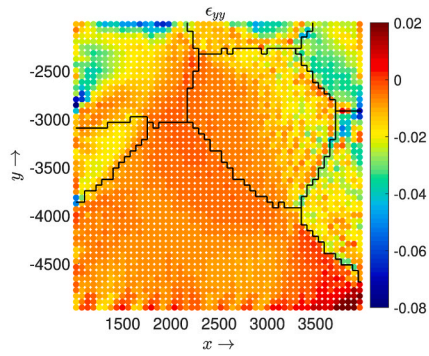
(b) ϵ_{yy} - 50 particles, 3 slices
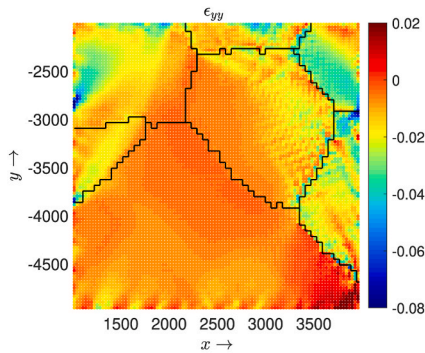
(c) ϵ_{yy} - 100 particles, 2 slices

(d) ϵ_{yy} - 100 particles, 3 slices

(e) ϵ_{yy} - 150 particles, 2 slices

(f) ϵ_{yy} - 150 particles, 3 slices
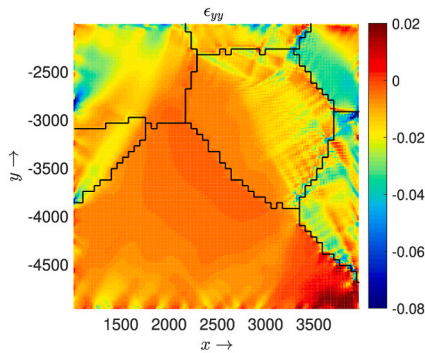
(g) ϵ_{yy} - 200 particles, 2 slices
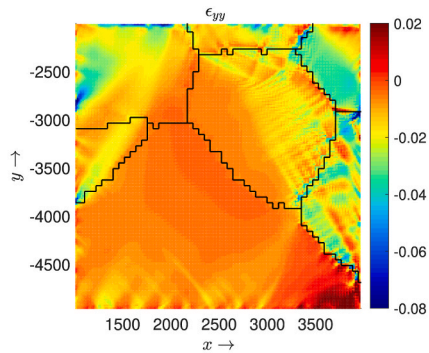
(h) ϵ_{yy} - 200 particles, 3 slices

(caption on next page)

Fig. 24. Strain component ε_{yy} visualized for different degrees of refinements and number of slices. The black segments denote grain boundaries. Units of length are μm.

3.4.1. Grain-averaged strains

Here, the predictions in strains components are compared quantitatively. Since the displacement components in 2D are recorded in the experiment, the data is post-processed to extract the in-plane strain components ε_{xx}, ε_{yy} and ε_{xy}. Fig. 20 shows the comparison in the three strain components between experiments and CPPD simulations with both discretizations. Figs. 23-25 depict the variation of x and y components of displacement respectively, for different degrees of refinement and number of slices. Qualitatively the strain fields look similar between experiments, CPPD and CPFE. To verify that the strain fields are also similar in an averaged sense, the mean strain fields in each grain are tabulated in Tables 9–11. Grains with their respective orientation IDs are depicted in Fig. 18(b).

Grain 42 is an outlier because it forms but a tiny fraction of the microstructure under consideration, so the grain-averaged strains are not reported (see Fig. 25). The tabulated results showcase, to some extent, the ability and efficacy of the CPPD framework to predict the grain averaged strain components. The grain-averaged normal strain predictions from CPPD show reasonable agreement with experimental results. The grain-averaged shear strains show a lot more variability in the percentage difference, especially since the values in the experiment are lower in magnitude due to which the relative differences can be high. The qualitative trends in the strain fields, when inspected visually, show comparable trends between CPPD and experiments in most regions of the microstructure. Clearly the experimental results are quite rich in that they show a number of localization patterns that are not captured by the simulation, which is expected since the crystal plasticity constitutive model doesn't take into account a host of phenomena occurring in the material. But on the level of the grain-averaged strains there is some promise that CPPD shows towards modeling elasto-plastic behavior of alloys. While both CPPD and CPFE show similar trends in the strain fields, CPPD resolves some strain localization patterns that are otherwise smoothed out by CPFE. Figs. 26–28 depict some of the regions in the simulated microstructure where band-like patterns are visible and well-resolved in CPPD.

4. Conclusions

In this paper, a 3D peridynamic implementation of CP is presented. This implementation introduces its novelty by combining key algorithmic features: an explicit time-stepping scheme with artificial damping, time-step selection procedure, higher-order stabilization of zero-energy modes and boundary condition implementation. The CPPD model is validated by comparing the deformation texture development in FCC-Cu and HCP-Mg 3D polycrystals under two different compression deformation modes. A 3D microstructure is simulated with two different horizon sizes to investigate the displacement and strain field predictions between the different horizon sizes. This is followed by a comparison of CPPD and CPFE simulation of a polycrystal with purely basal slip, depicting qualitative agreement between the two implementations and some signatures of localization in grains with low Schmid factor. Finally, CPPD predictions are compared against a recent SEM-DIC experiment of uniaxial tension in a magnesium WE43 alloy where the grain-averaged strains and localization patterns are compared. Normal components of the grain-averaged strains showed an overall agreement, and minor discrepancies are attributed to the localization patterns being predicted differently via experiments and simulations. Furthermore, CPPD results depict strain localization patterns which are typically well-resolved with increased refinement, otherwise smoothed out by CPFE. All the codes and examples constituting the current CPPD implementation will be available in an open source platform to the community upon publication of the work.

CRediT authorship contribution statement

Aaditya Lakshmanan: Conceptualization, Methodology, Software, Validation, Formal analysis, Investigation, Writing – original draft, Writing – review & editing, Visualization. **Jiangyi Luo:** Conceptualization, Methodology, Software, Validation, Formal analysis, Investigation, Writing – review & editing, Visualization. **Iman Javaheri:** Writing – original draft, Writing – review & editing, Funding acquisition. **Veera Sundararaghavan:** Conceptualization, Methodology, Formal analysis, Resources, Supervision, Writing – review & editing, Project administration, Funding acquisition.
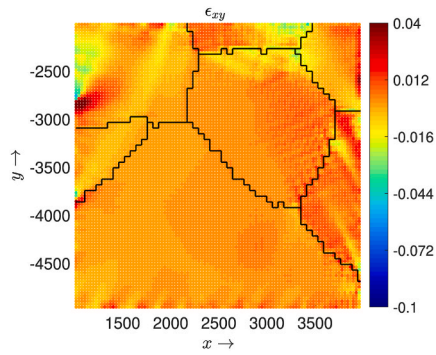
Declaration of competing interest

The authors declare that they have no known competing financial interests or personal relationships that could have appeared to influence the work reported in this paper.
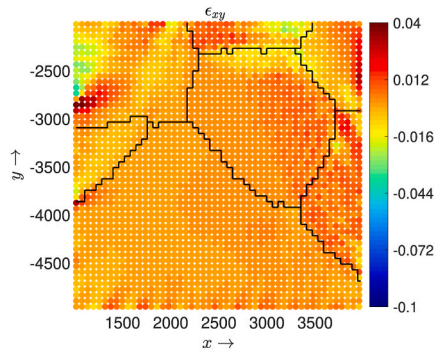
(a) ϵ_{xy} - 50 particles, 2 slices
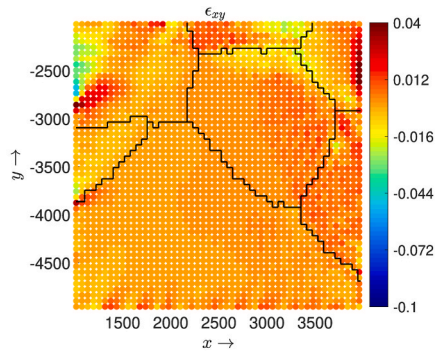
(b) ϵ_{xy} - 50 particles, 3 slices

(c) ϵ_{xy} - 100 particles, 2 slices
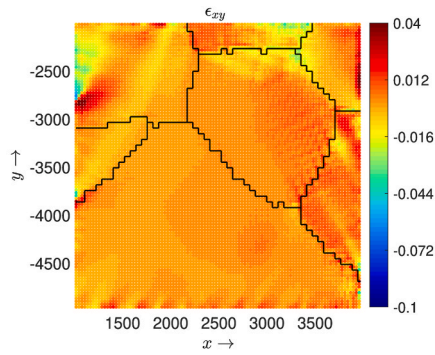
(d) ϵ_{xy} - 100 particles, 3 slices
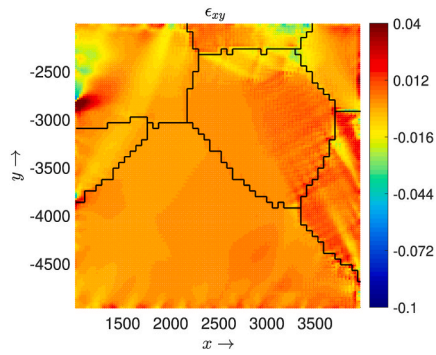
(e) ϵ_{xy} - 150 particles, 2 slices
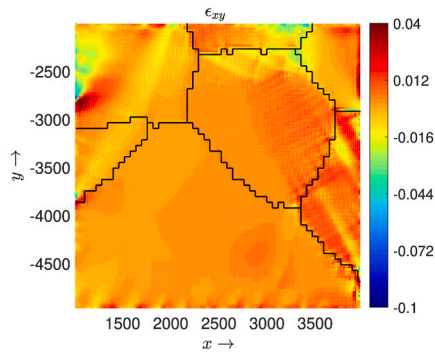
(f) ϵ_{xy} - 150 particles, 3 slices
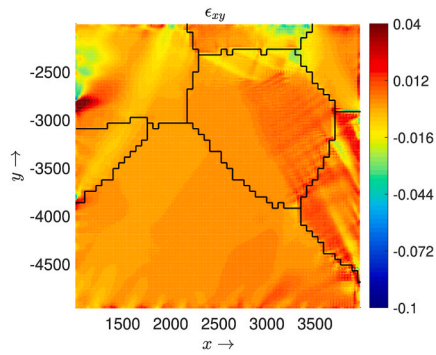
(g) ϵ_{xy} - 200 particles, 2 slices
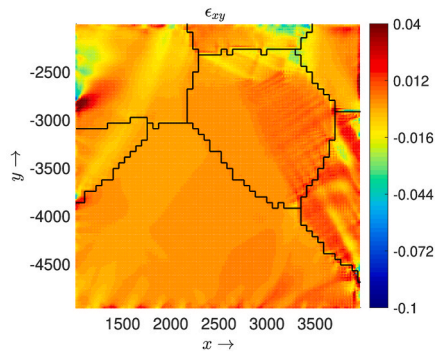
(h) ϵ_{xy} - 200 particles, 3 slices

(caption on next page)

Fig. 25. Strain component ε_{xy} visualized for different degrees of refinements and number of slices. The black segments denote grain boundaries. Units of length are μm.

Table 9
Comparison of grain-averaged strain component ε_{xx}.

Grain ID	ε_{xx}(Exp)	ε_{xx}(200)	Error(%)	ε_{xx}(CPFE)	Error(%)
13	0.04098	0.0345	15.847	0.0341	16.863
14	0.03446	0.0313	9.311	0.0364	5.672
16	0.04336	0.0682	57.367	0.0635	46.458
19	0.02124	0.0183	13.895	0.0136	35.812
23	0.02842	0.0425	49.544	0.0364	28.067
27	0.01915	0.0208	8.643	0.0287	50.092
28	0.01784	0.0147	17.415	0.0159	10.894

Table 10
Comparison of grain-averaged strain component ε_{yy}.

Grain ID	ε_{yy}(Exp)	ε_{yy}(200)	Error(%)	ε_{yy}(CPFE)	Error(%)
13	−0.02160	−0.0177	17.899	−0.01767	18.148
14	−0.01450	−0.0176	21.632	−0.01432	1.18
16	−0.02024	−0.0269	32.821	−0.0251	24.349
19	−0.01200	−0.0122	1.343	−0.00903	24.685
23	−0.01860	−0.0220	18.172	−0.0208	11.595
27	−0.00714	−0.0145	103.235	−0.0172	140.236
28	−0.00716	−0.0047	33.709	−0.00652	8.886

Table 11
Comparison of grain-averaged strain component ε_{xy}.

Grain ID	ε_{xy}(Exp)	ε_{xy}(200)	Error(%)	ε_{xy}(CPFE)	Error(%)
13	0.008463	−0.00653	177.177	0.00458	45.774
14	−0.000586	−0.00383	553.695	0.000236	140.304
16	0.000837	−0.00121	243.975	−0.00187	323.62
19	0.002951	0.00191	35.240	0.00117	60.258
23	0.007106	0.00495	30.307	0.00397	44.096
27	0.001594	−0.00258	261.481	−0.00506	417.391
28	0.000337	0.00160	375.896	0.0003002	109.061

(a) ϵ_{xx} - CPPD   (b) ϵ_{xx} - CPFE
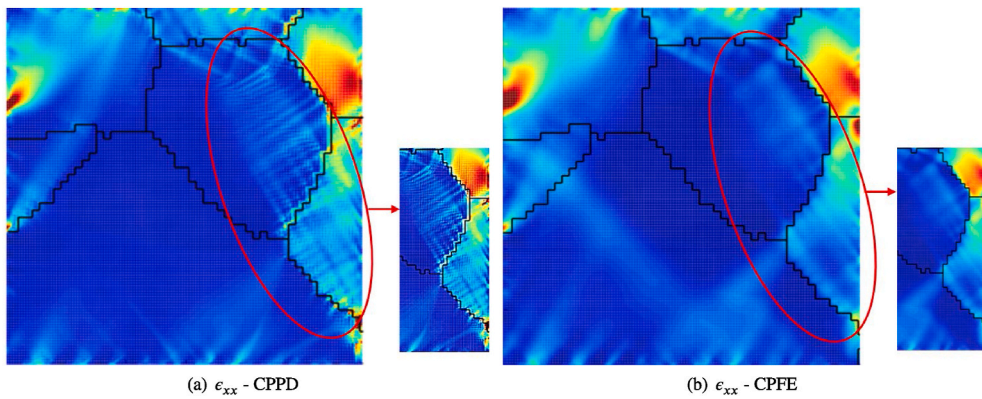
Fig. 26. Localization comparison for ε_{xx} between CPPD and CPFE.

(a) ϵ_{yy} - CPPD   (b) ϵ_{yy} - CPFE
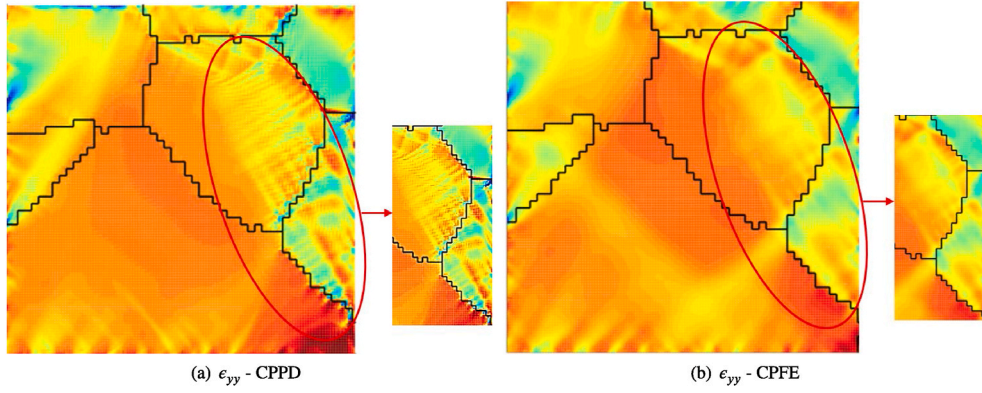
Fig. 27. Localization comparison for ε_{yy} between CPPD and CPFE.

(a) ϵ_{xy} - CPPD   (b) ϵ_{xy} - CPFE
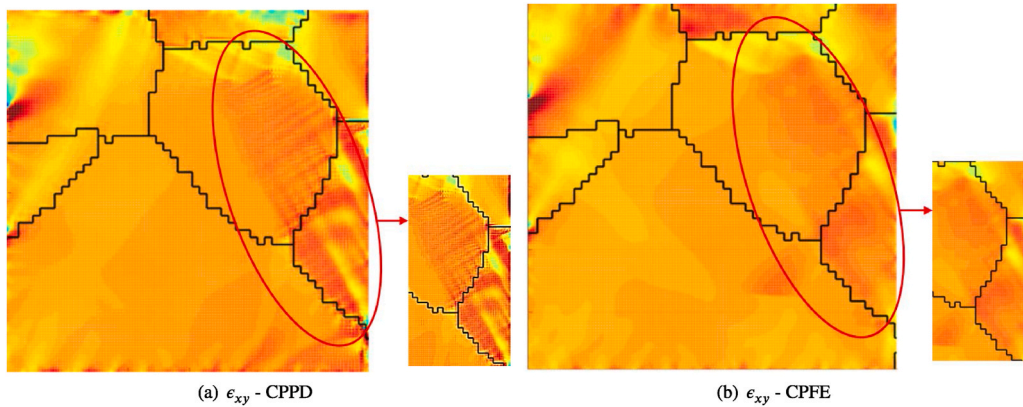
Fig. 28. Localization comparison for ε_{xy} between CPPD and CPFE.

Acknowledgements

Appendix A. Supplementary data

Supplementary data to this article can be found online at https://doi.org/10.1016/j.ijplas.2021.102991.

Appendix B. Crystal plasticity constitutive update scheme

All quantities below are described relative to the undeformed (also known as reference) configuration, and quantities at the current time step are denoted by subscript $(n + 1)$. Given the deformation gradient $\mathbf{F}_{n+1}$, the update procedure below numerically computes the PK-I stress (numerically converged) $\mathbf{P} = \mathcal{F}(\mathbf{F}_{n+1})$, where the operator $\mathcal{F}$ denotes the constitutive model. Implicit time integration scheme of (21) results in the following approximation with the additional assumption that $\Delta\gamma \ll 1$:

$$\mathbf{F}^{\mathrm{p}} = \exp\left(\Delta t \sum_\alpha \dot{\gamma}^\alpha \mathbf{S}_0^\alpha \mathrm{sign}(\tau^\alpha)\right)\mathbf{F}_n^{\mathrm{p}} \approx \left(\mathbf{I} + \sum_\alpha \Delta\gamma^\alpha \mathbf{S}_0^\alpha \mathrm{sign}(\tau^\alpha)\right)\mathbf{F}_n^{\mathrm{p}} \tag{B.1}$$

where $\Delta\gamma^\alpha = \dot{\gamma}^\alpha \Delta t$. Substituting Eqn. (B.1) into the multiplicative decomposition relation $\mathbf{F} = \mathbf{F}^{\mathrm{e}}\mathbf{F}^{\mathrm{p}}$ and rearranging terms yields:

$$\mathbf{F}^{e} = \mathbf{F}^{e}_{\text{trial}}\left(\mathbf{I} - \sum_{\alpha}\Delta\gamma^{\alpha}\mathbf{S}^{\alpha}_{0}\text{sign}(\tau^{\alpha})\right)$$ (B.2)

where $\mathbf{F}^{e}_{\text{trial}} = \mathbf{F}_{n+1}\mathbf{F}^{p-1}_{n}$ is the trial elastic deformation gradient. The initial condition $\mathbf{F}^{p}(0) = \mathbf{I}$ signifies that the reference configuration is plastically undeformed. The Green-Lagrange elastic strain measure computed using Eqn. (B.2) then takes the form:

$$\overline{\mathbf{E}}^{e} = \frac{1}{2}\left(\mathbf{F}^{eT}\mathbf{F}^{e} - \mathbf{I}\right) = \overline{\mathbf{E}}^{e}_{\text{trial}} - \frac{1}{2}\sum_{\alpha}\Delta\gamma^{\alpha}\mathbf{B}^{\alpha}\text{sign}(\tau^{\alpha})$$ (B.3)

where $\overline{\mathbf{E}}^{e}_{\text{trial}}$ and $\mathbf{B}^{\alpha}$ are defined as:

$$\overline{\mathbf{E}}^{e}_{\text{trial}} = \frac{1}{2}\left(\left(\mathbf{F}^{e}_{\text{trial}}\right)^{T}\mathbf{F}^{e}_{\text{trial}} - \mathbf{I}\right),$$ (B.4)

$$\mathbf{B}^{\alpha} = \left(\mathbf{S}^{\alpha}_{0}\right)^{T}\left(\mathbf{F}^{e}_{\text{trial}}\right)^{T}\mathbf{F}^{e}_{\text{trial}} + \left(\mathbf{F}^{e}_{\text{trial}}\right)^{T}\mathbf{F}^{e}_{\text{trial}}\mathbf{S}^{\alpha}_{0}$$ (B.5)

Using Eqn. (B.3) the intermediate stress $\overline{\mathbf{T}} = \mathcal{L}^{e}\cdot\overline{\mathbf{E}}^{e}$ takes the form:

$$\overline{\mathbf{T}} = \overline{\mathbf{T}}_{\text{trial}} - \frac{1}{2}\sum_{\alpha}\Delta\gamma^{\alpha}\mathcal{L}^{e}\cdot\mathbf{B}^{\alpha}\text{sign}(\tau^{\alpha}_{\text{trial}})$$ (B.6)

where $\overline{\mathbf{T}}_{\text{trial}} = \mathcal{L}^{e}\cdot\overline{\mathbf{E}}^{e}_{\text{trial}}$.

A trial resolved shear stress $\tau^{\alpha}_{\text{trial}} = \overline{\mathbf{T}}_{\text{trial}} : \mathbf{S}^{\alpha}_{0}$ is then computed so that potentially active set of slip systems (denoted as $\mathcal{PA}$) may be identified based on the criterion that $|\tau^{\alpha}_{\text{trial}}| - s^{\alpha} > 0$. The active systems (for which $\dot{\gamma}^{\alpha} > 0$) are assumed to follow the Kuhn-Tucker consistency condition: $|\tau^{\alpha}| = s^{\alpha}$. Substituting Eqn. (B.6) into the consistency yields:

$$|\tau^{\alpha}| = s^{\alpha} \Longrightarrow |\tau^{\alpha}_{\text{trial}}| - \frac{1}{2}\text{sign}(\tau^{\alpha}_{\text{trial}})\left(\sum_{\beta}\Delta\gamma^{\beta}\mathcal{L}^{e}\cdot\mathbf{B}^{\beta}\text{sign}(\tau^{\beta}_{\text{trial}})\right) : \mathbf{S}^{\alpha}_{0} = s^{\alpha}_{n} + \sum_{\beta}h^{\alpha\beta}(s^{\beta})\Delta\gamma^{\beta}$$

$$\Longrightarrow \left(h^{\alpha\beta} + \frac{1}{2}\text{sign}(\tau^{\alpha}_{\text{trial}})\text{sign}(\tau^{\beta}_{\text{trial}})(\mathcal{L}^{e}\cdot\mathbf{B}^{\beta}) : \mathbf{S}^{\alpha}_{0}\right)\Delta\gamma^{\beta} = |\tau^{\alpha}_{\text{trial}}| - s^{\alpha}$$

where $\alpha, \beta \in \mathcal{PA}$ and it is assumed that $\text{sign}(\tau^{\alpha}) = \text{sign}(\tau^{\alpha}_{\text{trial}})$. When the consistency conditions are written out for all the potentially active slip systems we obtain the following linear system:

$$\sum_{\beta\in\mathcal{PA}}A^{\alpha\beta}\Delta\gamma^{\beta} = b^{\alpha}$$ (B.7)

where

$$A^{\alpha\beta} = h^{\alpha\beta} + \frac{1}{2}\text{sign}\left(\tau^{\alpha}_{\text{trial}}\right)\text{sign}\left(\tau^{\beta}_{\text{trial}}\right)(\mathcal{L}^{e}\cdot\mathbf{B}^{\beta}) : \mathbf{S}^{\alpha}_{0},$$
$$b^{\alpha} = \left|\tau^{\alpha}_{\text{trial}}\right| - s^{\alpha}$$ (B.8)

Once the linear system is solved, a consistency check is performed to determine whether the potentially active systems are active, i. e., if $\Delta\gamma^{\beta} \geq 0 \ ; \ \forall\beta \in \mathcal{PA}$. Any system which fails consistency is removed from the set of potentially active systems. The entire procedure is repeated until $\Delta\gamma^{\beta} > 0 \ ; \ \forall\beta \in \mathcal{PA}$ at which point the potentially active slip systems are indeed active.

References

Acar, P., Ramazani, A., Sundararaghavan, V., 2017. Crystal plasticity modeling and experimental validation with an orientation distribution function for Ti-7Al alloy. Metals 7, 459.

Acar, P., Sundararaghavan, V., 2016. Utilization of a linear solver for multiscale design and optimization of microstructures. AIAA J. 54, 1751–1759.

Acharya, A., Bassani, J., Beaudoin, A., 2003. Geometrically necessary dislocations, hardening, and a simple gradient theory of crystal plasticity. Scripta Mater. 48, 167–172.

Agwai, A., Guven, I., Madenci, E., 2011. Predicting crack propagation with peridynamics: a comparative study. Int. J. Fract. 171, 65–78.

Anand, L., Kalidindi, S.R., 1994. The process of shear band formation in plane strain compression of FCC metals: effects of crystallographic texture. Mech. Mater. 17, 223–243.

Anand, L., Kothari, M., 1996. A computational procedure for rate-independent crystal plasticity. J. Mech. Phys. Solid. 44, 525–558.

Armero, F., Garikipati, K., 1996. An analysis of strong discontinuities in multiplicative finite strain plasticity and their relation with the numerical simulation of strain localization in solids. Int. J. Solid Struct. 33, 2863–2885.

Bazant, Z.P., Belytschko, T.B., Chang, T.P., 1984. Continuum theory for strain-softening. J. Eng. Mech. 110, 1666–1692.

Breitenfeld, M.S., Geubelle, P.H., Weckner, O., Silling, S.A., 2014. Non-ordinary state-based peridynamic analysis of stationary crack problems. Comput. Methods Appl. Mech. Eng. 272, 233–250.

Calcagnotto, M., Ponge, D., Demir, E., Raabe, D., 2010. Orientation gradients and geometrically necessary dislocations in ultrafine grained dual-phase steels studied by 2D and 3D EBSD. Mater. Sci. Eng., A 527, 2738–2746.

Cermelli, P., Gurtin, M.E., 2001. On the characterization of geometrically necessary dislocations in finite plasticity. J. Mech. Phys. Solid. 49, 1539–1568.

Counts, W.A., Braginsky, M.V., Battaile, C.C., Holm, E.A., 2008. Predicting the Hall-Petch effect in fcc metals using non-local crystal plasticity. Int. J. Plast. 24, 1243–1263.

Dawson, P.R., Marin, E.B., 1997. Computational mechanics for metal deformation processes using polycrystal plasticity. In: Advances in Applied Mechanics, vol. 34. Elsevier, pp. 77–169.

Dayal, K., Bhattacharya, K., 2006. Kinetics of phase transformations in the peridynamic formulation of continuum mechanics. J. Mech. Phys. Solid. 54, 1811–1842.

Dimiduk, D.M., Woodward, C., LeSar, R., Uchic, M.D., 2006. Scale-free intermittent flow in crystal plasticity. Science 312, 1188–1190.

Echlin, M.P., Stinville, J.C., Miller, V.M., Lenthe, W.C., Pollock, T.M., 2016. Incipient slip and long range plastic strain localization in microtextured Ti-6Al-4V titanium. Acta Mater. 114, 164–175.

Evers, L.P., Brekelmans, W.A.M., Geers, M.G.D., 2004. Scale dependent crystal plasticity framework with dislocation density and grain boundary effects. Int. J. Solid Struct. 41, 5209–5230.

Ganesan, S., 2017. Microstructural Response of Magnesium Alloys: 3D Crystal Plasticity and Experimental Validation. Ph.D. thesis. University of Michigan, Ann Arbor.

Ganesan, S., Yaghoobi, M., Githens, A., Chen, Z., Daly, S., Allison, J.E., Sundararaghavan, V., 2021. The effects of heat treatment on the response of we43 mg alloy: crystal plasticity finite element simulation and sem-dic experiment. Int. J. Plast. 137, 102917.

Gerstle, W.H., 2015. Introduction to Practical Peridynamics: Computational Solid Mechanics without Stress and Strain, vol. 1. World Scientific Publishing Co Inc.

Githens, A., Ganesan, S., Chen, Z., Allison, J., Sundararaghavan, V., Daly, S., 2020a. Characterizing microscale deformation mechanisms and macroscopic tensile properties of a high strength magnesium rare-earth alloy: a combined experimental and crystal plasticity approach. Acta Mater. 186, 77–94.

Githens, A., Ganesan, S., Chen, Z., Allison, J., Sundararaghavan, V., Daly, S., 2020b. Characterizing microscale deformation mechanisms and macroscopic tensile properties of a high strength magnesium rare-earth alloy: a combined experimental and crystal plasticity approach. Acta Mater. 186, 77–94.

Greer, J.R., Oliver, W.C., Nix, W.D., 2005. Size dependence of mechanical properties of gold at the micron scale in the absence of strain gradients. Acta Mater. 53, 1821–1830.

Gu, X., Zhang, Q., Madenci, E., 2019. Non-ordinary state-based peridynamic simulation of elastoplastic deformation and dynamic cracking of polycrystal. Eng. Fract. Mech. 218, 106568.

Guery, A., Hild, F., Latourte, F., Roux, S., 2016. Slip activities in polycrystals determined by coupling DIC measurements with crystal plasticity calculations. Int. J. Plast. 81, 249–266.

Ha, Y.D., Bobaru, F., 2010. Studies of dynamic crack propagation and crack branching with peridynamics. Int. J. Fract. 162, 229–244.

Hallai, J.F., Kyriakides, S., 2013. Underlying material response for Lüders-like instabilities. Int. J. Plast. 47, 1–12.

Harren, S.V., Deve, H.E., Asaro, R.J., 1988. Shear band formation in plane strain compression. Acta Metall. 36, 2435–2480.

Hearmon, R.F.S., 1984. The elastic constants of crystals and other anisotropic materials. Landolt-Bornstein Tables III/18, 1154.

Hill, R., 1966. Generalized constitutive relations for incremental deformation of metal crystals by multislip. J. Mech. Phys. Solid. 14, 95–102.

Hill, R., Rice, J., 1972. Constitutive analysis of elastic-plastic crystals at arbitrary strain. J. Mech. Phys. Solid. 20, 401–413.

Hornbogen, E., Gahr, K.K.H.Z., 1975. Distribution of plastic strain in alloys containing small particles. Metallography 8, 181–202.

Jacobs, T.R., Matlock, D.K., Findley, K.O., 2019. Characterization of localized plastic deformation behaviors associated with dynamic strain aging in pipeline steels using digital image correlation. Int. J. Plast. 123, 70–85.

Javaheri, I., Sundararaghavan, V., 2020. Polycrystalline microstructure reconstruction using Markov random fields and histogram matching. Comput. Aided Des. 120, 102806.

Kammers, A.D., Daly, S., 2013. Digital image correlation under scanning electron microscopy: methodology and validation. Exp. Mech. 53, 1743–1761.

Khan, M.I.H., 2014. Shear Band Regularization with Peridynamics. Ph.D. thesis. The University of Texas at San Antonio.

Kilic, B., Madenci, E., 2010. An adaptive dynamic relaxation method for quasi-static simulations using the peridynamic theory. Theor. Appl. Fract. Mech. 53, 194–204.

LeVeque, R.J., 2007. Finite Difference Methods for Ordinary and Partial Differential Equations: Steady-State and Time-dependent Problems. SIAM.

Littlewood, D.J., 2011. A nonlocal approach to modeling crack nucleation in AA 7075-T651. In: ASME 2011 International Mechanical Engineering Congress and Exposition. American Society of Mechanical Engineers, pp. 567–576.

Liu, D., Dunstan, D., 2017. Material length scale of strain gradient plasticity: a physical interpretation. Int. J. Plast. 98, 156–174.

Liu, W., Yang, G., Cai, Y., 2018. Modeling of failure mode switching and shear band propagation using the correspondence framework of peridynamics. Comput. Struct. 209, 150–162.

Luo, J., 2019. Peridynamic Modeling of Crystal Plasticity with an Adaptive Dynamic Relaxation Solver. Ph.D. thesis. University of Michigan, Ann Arbor.

Luo, J., Ramazani, A., Sundararaghavan, V., 2018. Simulation of micro–scale shear bands using peridynamics with an adaptive dynamic relaxation method. Int. J. Solid Struct. 130, 36–48.

Luo, J., Sundararaghavan, V., 2018. Stress-point method for stabilizing zero-energy modes in non-ordinary state-based peridynamics. Int. J. Solid Struct.

Maaß, R., Petegem, S.V., Swygenhoven, H.V., Derlet, P.M., Volkert, C.A., Grolimund, D., 2007. Time-resolved laue diffraction of deforming micropillars. Phys. Rev. Lett. 99, 145505.

Macek, R.W., Silling, S.A., 2007. Peridynamics via finite element analysis. Finite Elem. Anal. Des. 43, 1169–1178.

Madenci, E., Oterkus, E., 2014. Peridynamic Theory and its Applications, vol. 17. Springer.

Mandel, J., 1973. Equations constitutives et directeurs dans les milieux plastiques et viscoplastiques. Int. J. Solid Struct. 9, 725–740.

Oliver, J., 1989. A consistent characteristic length for smeared cracking models. Int. J. Numer. Methods Eng. 28, 461–474.

Ren, H., Zhuang, X., Cai, Y., Rabczuk, T., 2016. Dual-horizon peridynamics. Int. J. Numer. Methods Eng. 108, 1451–1476.

Ruggles, T.J., Fullwood, D.T., 2013. Estimations of bulk geometrically necessary dislocation density using high resolution EBSD. Ultramicroscopy 133, 8–15.

Samaniego, E., Belytschko, T., 2005. Continuum–discontinuum modelling of shear bands. Int. J. Numer. Methods Eng. 62, 1857–1872.

Shaw, J.A., Kyriakides, S., 1997. Initiation and propagation of localized deformation in elasto-plastic strips under uniaxial tension. Int. J. Plast. 13, 837–871.

Silling, S.A., 2000. Reformulation of elasticity theory for discontinuities and long-range forces. J. Mech. Phys. Solid. 48, 175–209.

Silling, S.A., 2017. Stability of peridynamic correspondence material models and their particle discretizations. Comput. Methods Appl. Mech. Eng. 322, 42–57.

Silling, S.A., Askari, E., 2005. A meshfree method based on the peridynamic model of solid mechanics. Comput. Struct. 83, 1526–1535.

Silling, S.A., Epton, M., Weckner, O., Xu, J., Askari, E., 2007. Peridynamic states and constitutive modeling. J. Elasticity 88, 151–184.

Silling, S.A., Weckner, O., Askari, E., Bobaru, F., 2010. Crack nucleation in a peridynamic solid. Int. J. Fract. 162, 219–227.

Song, X., Menon, S., 2018. Modeling shear banding of three-phase geological materials with chemical effect through a novel non-local method. In: AGUFM 2018. MR41B–0059.

Staroselsky, A.V., 1998. Crystal Plasticity Due to Slip and Twinning. Ph.D. thesis. Massachusetts Institute of Technology.

Sun, S., Sundararaghavan, V., 2014a. A peridynamic implementation of crystal plasticity. Int. J. Solid Struct. 51, 3350–3360.

Sun, S., Sundararaghavan, V., 2014b. A peridynamic implementation of crystal plasticity. Int. J. Solid Struct. 51, 3350–3360.

Sundararaghavan, V., Zabaras, N., 2004. A dynamic material library for the representation of single-phase polyhedral microstructures. Acta Mater. 52, 4111–4119.

Sundararaghavan, V., Zabaras, N., 2007. Linear analysis of texture–property relationships using process-based representations of Rodrigues space. Acta Mater. 55, 1573–1587.

Sundararaghavan, V., Zabaras, N., 2009. A statistical learning approach for the design of polycrystalline materials. Stat. Anal. Data Min. 1, 306–321.

Teodosiu, C., 1997. Large Plastic Deformation of Crystalline Aggregates, vol. 376. Springer.

Tomé, C.N., Kaschner, G.C., 2005. Modeling texture, twinning and hardening evolution during deformation of hexagonal materials. In: Materials Science Forum. Trans Tech Publ, pp. 1001–1006.

Tupek, M.R., Radovitzky, R., 2014. An extended constitutive correspondence formulation of peridynamics based on nonlinear bond-strain measures. J. Mech. Phys. Solid. 65, 82–92.

Voyiadjis, G.Z., Song, Y., 2019. Strain gradient continuum plasticity theories: theoretical, numerical and experimental investigations. Int. J. Plast.

Warren, T.L., Silling, S.A., Askari, A., Weckner, O., Epton, M.A., Xu, J., 2009. A non-ordinary state-based peridynamic method to model solid material deformation and fracture. Int. J. Solid Struct. 46, 1186–1195.

Wu, C.T., Ben, B., 2015. A stabilized non-ordinary state-based peridynamics for the nonlocal ductile material failure analysis in metal machining process. Comput. Methods Appl. Mech. Eng. 291, 197–215.

Yaghoobi, A., Chorzepa, M.G., 2017. Higher–order approximation to suppress the zero-energy mode in non-ordinary state-based peridynamics. Comput. Struct. 188, 63–79.

Yaghoobi, M., Ganesan, S., Sundar, S., Lakshmanan, A., Rudraraju, S., Allison, J.E., Sundararaghavan, V., 2019. Prisms-plasticity: an open-source crystal plasticity finite element software. Comput. Mater. Sci. 169, 109078.

Yuzbekova, D., Mogucheva, A., Zhemchuzhnikova, D., Lebedkina, T., Lebyodkin, M., Kaibyshev, R., 2017. Effect of microstructure on continuous propagation of the portevin–le chatelier deformation bands. Int. J. Plast. 96, 210–226.

Zhang, J., Liu, G., Sun, J., 2013. Strain rate effects on the mechanical response in multi-and single-crystalline Cu micropillars: grain boundary effects. Int. J. Plast. 50, 1–17.

Zhang, M., Bridier, F., Villechaise, P., Mendez, J., McDowell, D.L., 2010. Simulation of slip band evolution in duplex Ti-6Al-4V. Acta Mater. 58, 1087–1096.